Chandra centres for COSMOS X-ray galaxy groups: differences in stellar properties between central dominant and offset brightest group galaxies

Journal Article

Author(s):
Gozaliasl, Ghassem; Finoguenov, Alexis; Tanaka, Masayuki; Dolag, Klaus; Montanari, Francesco; Kirkpatrick, Charles C.; Vardoulaki, Eleni; Khosroshahi, Habib G.; Salvato, Mara; Laigle, Clotilde; McCracken, Henry J.; Ilbert, Olivier; Cappelluti, Nico; Daddi, Emanuele; Hasinger, Günther; Capak, Peter; Scoville, Nicholas Z.; Toft, Sune; Civano, Francesca; Griffiths, Richard E.; Balogh, Michael; Li, Yanxia; Ahoranta, Jussi; Mei, Simona; Iovino, Angela; Henriques, Bruno M.B.; Erfanianfar, Ghazaleh

Chandra centres for COSMOS X-ray galaxy groups: differences in stellar properties between central dominant and offset brightest group galaxies

Ghassem Gozaliasl [ID],[1,2,3]★ Alexis Finoguenov [ID],[2]★ Masayuki Tanaka,[7]
Klaus Dolag,[11,12] Francesco Montanari,[2,3] Charles C. Kirkpatrick,[2] Eleni Vardoulaki,[6]
Habib G. Khosroshahi,[5] Mara Salvato [ID],[4] Clotilde Laigle,[17] Henry J. McCracken,[9]
Olivier Ilbert,[8] Nico Cappelluti,[10] Emanuele Daddi [ID],[13] Guenther Hasinger,[14]
Peter Capak,[15,16] Nick Z. Scoville,[18] Sune Toft,[28] Francesca Civano,[19]
Richard E. Griffiths,[20] Michael Balogh,[21] Yanxia Li,[22] Jussi Ahoranta,[2]
Simona Mei,[23,24,25] Angela Iovino,[26] Bruno M. B. Henriques [ID][27] and
Ghazaleh Erfanianfar[4]

Affiliations are listed at the end of the paper

ABSTRACT

We present the results of a search for galaxy clusters and groups in the ~ 2 deg^2 of the COSMOS field using all available X-ray observations from the *XMM–Newton* and *Chandra* observatories. We reach an X-ray flux limit of 3×10^{-16} erg cm^{-2} s^{-1} in the 0.5–2 keV range, and identify 247 X-ray groups with $M_{200c} = 8 \times 10^{12}$–$3 \times 10^{14}$ M$_\odot$ at a redshift range of $0.08 \leq z < 1.53$, using the multiband photometric redshift and the master spectroscopic redshift catalogues of the COSMOS. The X-ray centres of groups are determined using high-resolution *Chandra* imaging. We investigate the relations between the offset of the brightest group galaxies (BGGs) from halo X-ray centre and group properties and compare with predictions from semi-analytic models and hydrodynamical simulations. We find that BGG offset decreases with both increasing halo mass and decreasing redshift with no strong dependence on the X-ray flux and SNR. We show that the BGG offset decreases as a function of increasing magnitude gap with no considerable redshift-dependent trend. The stellar mass of BGGs in observations extends over a wider dynamic range compared to model predictions. At $z < 0.5$, the central dominant BGGs become more massive than those with large offsets by up to 0.3 dex, in agreement with model prediction. The observed and predicted log-normal scatter in the stellar mass of both low- and large-offset BGGs at fixed halo mass is ~ 0.3 dex.

Key words: galaxies: clusters: general – galaxies: evolution – galaxies: groups: general – galaxies: statistics – galaxies: stellar content – X-rays: galaxies: clusters.

1 INTRODUCTION

According to the standard scenario of galaxy formation, galaxies form via cooling and condensing gas at the bottom of the potential wells of a population of hierarchically merging dark matter haloes (White & Rees 1978). After a halo and its 'central' galaxy fall into a larger system, it becomes a subhalo and its galaxy becomes a 'satellite'. The cold gas of this satellite galaxy may be stripped,

leading to a sharp decline in star formation, reddening its colour. Strong tidal stripping can eject stars or even disrupt the satellite altogether, providing more material for the disc of the central galaxy of the massive halo and the stars' stellar halo. Consequently, the central galaxy can grow and become the most massive and luminous galaxy in the system (e.g. Springel et al. 2005; Skibba et al. 2010; Guo et al. 2011; Henriques et al. 2015, 2017).

Following this paradigm and the Λ-cold dark matter (ΛCDM) model, several semi-analytic models have been implemented using the Millennium simulations (I&II) (e.g. Springel et al. 2005; Bower et al. 2006; De Lucia & Blaizot 2007; Guo et al. 2011; Henriques et al. 2015). However, observations show that the 'central galaxy

paradigm' (CGP), which predicts that central galaxies are the most massive and brightest cluster/group galaxies, is not always true (Beers & Geller 1983; Sanderson, Edge & Smith 2009; Skibba et al. 2010). Skibba et al. (2010) analysed the offsets of the line-of-sight velocities and projected positions of brightest group galaxies (BGGs) relative to the other group members using the Sloan Digital Sky Survey (SDSS) cluster catalogue of Yang et al. (2007) and ruled out the CGP.

The assumption of CGP is critical in a number of measurements such as halo mass estimates using satellite kinematics (e.g. More et al. 2008), strong and weak lensing (e.g. Kochanek 1995; Sheldon et al. 2009), halo occupation modelling (Tinker et al. 2008), and algorithms for identifying groups (Yang et al. 2007; Yang, Mo & Van den Bosch 2009; Yang et al. 2012). It is also well known that central galaxies exhibit different characteristics such as size, morphology, colour, star formation, radio, and active galactic nucleus (AGN) activities compared to the satellite galaxies of the same stellar mass. The dependence of the central galaxy properties on the halo properties such as halo mass has been found to be strong (De Lucia & Blaizot 2007; Van Den Bosch et al. 2008; Skibba & Sheth 2009; Gozaliasl et al. 2014a, 2016, 2018). Admittedly, these results suggest that a precise definition of central galaxies is essential for a precise modelling of galaxies and interpreting the observational results. This paper investigates the validity of the CGP in X-ray galaxy groups quantifying the offset of the projected positions of BGGs relative to the peak of the X-ray emissions from the intragroup hot gas and medium.

Galaxy evolution is thought to be the result of halo growth, as well as several other galaxy formation processes (e.g. star formation, feedback from star formation and AGN), and environmental effects. To recognize the role of various physical processes of galaxy formation and to link galaxies to their dark matter haloes, studies look for the relation between the halo mass function and the stellar mass function. The stellar-to-halo mass relation is thought to be related to the star formation efficiency, and to the strength of feedback from star formation and AGN. It has broadly been studied as a function of time using several techniques such as matching the abundances of observed galaxies and simulated dark haloes ranked by stellar and dark matter mass (Behroozi, Conroy & Wechsler 2010; Moster, Naab & White 2013), the conditional luminosity function method proposed by Yang et al. (2012), by the halo occupation distribution (HOD) formalism (Moster et al. 2010; Behroozi, Wechsler & Conroy 2013; Moster et al. 2013), and by combining the HOD, *N*-body simulations, galaxy clustering, and galaxy–galaxy lensing techniques (Leauthaud et al. 2012; Coupon et al. 2015).

Observations indicate that there is a strong correlation between the stellar mass of central galaxies and halo mass of hosting haloes, particularly at low halo masses ($M_{200} \lesssim 10^{12}\,M_{\odot}$). The stellar mass of satellite galaxies does not show such a dependence on halo mass. Both observations and simulations indicate the presence of a large scatter in the stellar mass of central galaxies at fixed halo mass (Moster et al. 2010; Behroozi et al. 2010, 2013; Coupon et al. 2015; Matthee et al. 2017).

Several studies (e.g. Behroozi et al. 2010; Coupon et al. 2015; Matthee et al. 2017) have searched for the origin of this scatter and have quantified the different sources of systematic errors, such as varying the assumed cosmology, initial mass function, the stellar population model (SPE), and the dust attenuation laws. Despite these efforts, the inconsistencies between the observational data and model predictions illustrate that scatter in the stellar mass of central galaxies is still an unresolved problem. However, the effect of CGP on the scatter of stellar mass has not been enunciated yet,

while it is well known that the properties of galaxies change with increasing the offset between the galaxy position and the centre of clusters. The primary goal of this study is to address the presence of an offset between the coordinate of the most massive galaxy and the position of the X-ray peak. We construct the stellar mass distribution and compare the corresponding distribution for BGGs with low and high offsets from the group X-ray centres. We also examine the impact of the offset on the scatter in the stellar mass of the central massive galaxies at fixed halo masses.

The COSMOS survey covers ∼2 deg² equatorial field and was designed to probe the formation and evolution of galaxies, star formation, AGN, and dark matter with large-scale structure (LSS) as a function of local galaxy environment and redshift out to $z = 6$ (Scoville et al. 2007). The COSMOS survey has been observed by a number of major space- and ground-based telescopes, notably by the *XMM–Newton*, *Chandra*, *HST*, *GALEX*, MIPS/*Spitzer*, PACS/*Herschel* and SPIRE/*Herschel*, VISTA, and SUBARU telescopes, and offers a unique combination of deep ($AB \sim 25$–26), multiwavelength data (0.25 μm ⟼ 24 μm). We use the COSMOS2015 catalogue of photometric redshifts of over half a million sources with an excellent precision of $\sigma_{\Delta z/(1+z_s)} = 0.007$ (Laigle, Capak & Scoville 2016). The COSMOS field has frequently been of the focus of spectroscopic redshift surveys. The unique data of spectroscopic and multiband photometric redshifts of galaxies together with the X-ray data provided by *Chandra* COSMOS-Legacy Survey (Elvis et al. 2009; Civano et al. 2016; Marchesi et al. 2016) and *XMM–Newton* observations allow us to revise the detection of X-ray galaxy groups and clusters in COSMOS as previously presented by Finoguenov et al. (2007) and George et al. (2011). This study aims to improve the determination of the position of the X-ray peak (centre) and the redshift of groups and clusters.

This study presents a unique catalogue of 247 X-ray groups of galaxies identified in 2 deg² of the COSMOS field (Scoville et al. 2007) at a redshift range of $0.08 \leq z < 1.53$ with a mass range of $M_{200c} = 8 \times 10^{12}$–$3 \times 10^{14}\,M_{\odot}$. High-mass systems in this halo-mass range are on the border line between groups and clusters but for the purpose of this paper we will refer to these systems only as groups. We select the most massive group galaxies within R_{200} (where the internal density of haloes is 200 times the critical density of the Universe). Since the most massive group galaxies are generally the most luminous group galaxies, we will refer to these galaxies as BGGs in this study. We quantify the projected separation between the position of BGGs and the IGM X-ray emission peaks, defining the BGG offset as the ratio of this angular separation to the group's R_{200} and estimate differences between the stellar properties of the central dominant BGGs and the BGGs with large offsets. We interpret our observational results through a comparison with predictions from two semi-analytic models (SAMs) implemented based on the output data of the Millennium simulations by Guo et al. (2011, hereafter G11) and Henriques et al. (2015, hereafter H15). In addition, for the comparison of our observational results with those from hydrodynamical simulations, we use BGGs and galaxy groups selected from the Magneticum Pathfinder simulation,[1] which adopts a WMAP7 (Komatsu et al. 2011) cosmology (Dolag et al. in preparation).

This paper is organized as follows. In Section 2, we describe the catalogues of the spectroscopic and photometric redshift of galaxies used in this study. Section 3 describes the procedures for identification of groups, revision of the X-ray centre and redshift of

---

[1]www.magneticum.org

groups, and a description of the new catalogue of groups. Section 4 presents the sample definition, the BGG selection, the BGG offset from the X-ray centroid, the evolution, and distribution of the BGG offset. It also presents the relations between the offset with halo mass, the X-ray flux, and the magnitude gap between the first and second ranked BGGs. Section 5 presents the differences in the stellar mass of BGGs selected within different aperture sizes: $0.5R_{500}, R_{500}$, and R_{200}. It also presents the non-parametric distribution of the stellar mass and the scatter in the stellar mass of BGGs. Section 6 summarizes the results and conclusions.

Unless stated otherwise, we adopt a cosmological model, with $(\Omega_\Lambda, \Omega_M, h) = (0.70, 0.3, 0.71)$, where the Hubble constant is parametrized as $100\,h\,\mathrm{km\,s^{-1}\,Mpc^{-1}}$, and quote uncertainties at the 68 per cent confidence level.

2 THE COSMOS SURVEY DATA

2.1 The COSMOS survey

The Cosmological Evolution Survey (COSMOS) is a deep multi-band survey centred at (Ra, Dec) = (+150.1192, +2.2058) and covering a 2 deg^2 area. The full definition and survey goals can be found in Scoville et al. (2007).

COSMOS is the largest field that has been observed by the *Hubble Space telescope* (*HST*) so far. In addition, COSMOS guarantees full spectral coverage with multiwavelength imaging and spectroscopy from X-ray to radio wavelengths by the major space-based telescopes (*Hubble*, *Spitzer*, *GALEX*, *XMM*, *Chandra*, *Herschel*, and *NuStar*) and the large ground-based observatories (Keck, Subaru, VLA, ESO-VLT, UKIRT, NOAO, CFHT, JCMT, ALMA, and others).[2]

Over 2 million galaxies have been detected in the deep optical images (e.g. *i* band) (Ilbert et al. 2008), and 1.2 million in the NIR (Laigle et al. 2016), spanning over 2/3 of cosmic time. The Cosmic Assembly Near-infrared Deep Extragalactic Legacy Survey (CANDELS) is also a part of this field that has been surveyed deeper in the NIR with *HST* (Nayyeri et al. 2017). The unique multiwavelengths data set of COSMOS enables a precise determination of the photometric redshift of galaxies (e.g. Laigle et al. 2016). It allows us to study the star formation history and AGNs over $z = 0.5$–6 (e.g. Karim et al. 2011; Ceraj et al. 2018). Furthermore, the multibands data enable us to detect galaxy groups and clusters (Finoguenov et al. 2007; George et al. 2011), protoclusters, and X-ray group from the core of a high-z protocluster (Wang et al. 2016).

2.2 The COSMOS spectroscopic redshift surveys

COSMOS is a unique field in its unparalleled spectroscopic observations. Since 2007, a number of spectroscopic follow-up campaigns have been accomplished in the COSMOS field (e.g. Lilly et al. 2007; Kartaltepe et al. 2010; Comparat et al. 2015; Le Fèvre et al. 2015). The spectroscopic observations of the COSMOS galaxies are still ongoing and Hasinger et al. (2018) present more recently spectroscopic redshifts for 10 718 objects in the COSMOS field, observed through multislit spectroscopy with the Deep Imaging Multi-Object Spectrograph (DEIMOS) on the Keck II telescope in

the wavelength range ∼550–980 nm. The catalogue contains 6617 objects with high-quality spectra (two or more spectral features), and 1798 objects with a single spectroscopic feature confirmed by the photometric redshift.

Table 1 provides a list of important characteristics of the spectroscopic redshift surveys. Columns 1 and 2 list the survey name/reference and instrument/telescopes, respectively. Columns 3, 4, and 5 report the number of objects with secure redshift determination, the median redshift, and the redshift range of the survey, respectively. Column 6 shows the median i^+ band magnitude of galaxies for each survey (Laigle et al. 2016; Hasinger et al. 2018).

In this study, we use an updated catalogue of 36 274 galaxies with secure spectroscopic redshifts by M. Salvato et al. (in preparation) and Hasinger et al. (2018) to determine the redshift of our groups, when possible.

2.3 The COSMOS photometric redshifts

When there are not enough galaxies with spectroscopic redshifts within an extended X-ray source to update the redshift of associated group, we revise the redshift of this source and its group using recent photometric redshifts catalogues, notably, the COSMOS2015 catalogue (Laigle et al. 2016) and the earlier catalogues presented in Ilbert et al. (2008), McCracken et al. (2012), and Ilbert et al. (2013). All these catalogues use the SED-fitting method and apply the *le Phare* code to measure the photometric redshifts and stellar masses with a χ^2 template-fitting method. The details of the method can be found in Ilbert et al. (2008) and Ilbert et al. (2013).

The COSMOS2015 catalogue contains precise photometric redshifts and stellar masses for over half a million sources. The object detection in this catalogue has been done using $YJHK_s$ data from the UltraVISTA-DR2 survey. However, for the better estimate of the photometric redshifts, a combination of 31 band data has been used. A summary of available data in each band, the average limiting magnitudes, and the central wavelength of each band has been presented in table 1 of Laigle et al. (2016). The COSMOS2015 catalogue is also a unique catalogue in terms of the accuracy of photometric redshifts. Using a secure sample of spectroscopic redshifts such as zCOSMOS-bright (see Table 1), the precision of the photo-z of galaxies is found to reach $\sigma_{\Delta z/(1+z_s)} = 0.007$ with a catastrophic failure fraction of $\eta = 0.5$ per cent. At $3 < z < 6$, the photo-z precision was obtained as $\sigma_{\Delta z/(1+z_s)} = 0.021$. Section 4.3 and fig. 11 in Laigle et al. (2016) present a detailed analysis on the accuracy of the photo-z for two types of star-forming and quiescent galaxies with different i-band magnitude ranges from 16 to 27 mag. This figure is in agreement with fig. 8 in Ilbert et al. (2006), who indicate that the spectral type is not the dominant factor, and that the redshift and the magnitude are more relevant to the photo-z accuracy. We emphasize that early-type galaxies produce a lower quality photo-z (in both Laigle et al. 2016 and Ilbert et al. 2006 analyses), probably, because we do not have a sufficiently large variety of templates for this population.

The COSMOS2015 catalogue covers effective areas of 0.46 deg^2 Ultra deep and 0.92 deg^2 of deep UltraVISTA surveys. At the deepest regions, the stellar mass of galaxies reaches a 90 per cent completeness limit of $10^{10}\,\mathrm{M_\odot}$ to $z = 4.0$. Details of these regions can be found in section 7.1 (fig. 1 and table 7) by Laigle et al. (2016). For more details on the photo-z estimate and the stellar mass estimation, we refer the reader to Laigle et al. (2016).

For maximizing catalogue completeness for bluer objects and at higher redshifts, Laigle et al. (2016) detected objects on a χ^2 sum of the $YJHK_s$ and Subaru SUPRIME-CAM broad-band

---

[2]For more information on the COSMOS multiwavelengths observations, the list of broad-, intermediate-, and narrow-band filters, and the filter transmissions that are used by COSMOS, we refer readers to the COSMOS home web page (http://cosmos.astro.caltech.edu/).

Table 1. Characteristics of the spectroscopic redshift samples. Only the most secure spectroscopic redshifts are considered (those with a flag between 3 and 4). The redshift range, median redshift, and apparent magnitude in the band are provided for each selected sample.

Spectroscopic survey reference	Instrument/telescope	N_b	z_{med}	z_{range}	i^+_{med}
zCOSMOS-bright (Lilly et al. 2007)	VIMOS/VLT	8608	0.48	[0.02, 1.19]	21.6
Comparat et al. (2015)	FORS2/VLT	788	0.89	[0.07, 3.65]	22.6
P. Capak et al. (in preparation); Kartaltepe et al. (2010)	DEIMOS/Keck II	2022	0.93	[0.02, 5.87]	23.2
Roseboom et al. (2012)	FMOS/Subaru	26	1.21	[0.82, 1.50]	22.5
Onodera et al. (2012)	MOIRCS/Subaru	10	1.41	[1.24, 2.09]	23.9
FMOS-COSMOS (Silverman et al. 2015)	FMOS/Subaru	178	1.56	[1.34, 1.73]	23.5
WFC3-grism (Krogager et al. 2014)	WFC3/HST	11	2.03	[1.88, 2.54]	25.1
zCOSMOS-deep (S. Lilly et al. in preparation)	VIMOS/VLT	767	2.11	[1.50, 2.50]	23.8
MOSDEF (Kriek et al. 2015)	MOSFIRE/Keck I	80	2.15	[0.80, 3.71]	24.2
M. Stockmann et al. (in preparation); Zabl (2015)	XSHOOTER/VLT	14	2.19	[1.98, 2.48]	22.2
VUDS (Le Fèvre et al. 2015)	VIMOS/VLT	998	2.70	[0.10, 4.93]	24.6
DEIMOS 10K (Hasinger et al. 2018)	DEIMOS/Keck II	6617	1 and 4	[0.00, 6.00]	23

z^{++} (central wavelength of 910.572 nm) images. However, this catalogue misses around 25 per cent of blue objects that were detected in the *i*-selected catalogue by Ilbert et al. (2008). Thus, for a complete identification of groups within the whole $\sim 2\,deg^2$ area of the COSMOS field and a complete selection of group members, besides the COSMOS2015 catalogue, we utilize the earlier *i*-band selected v.2 catalogue of photometric redshifts by Ilbert et al. (2008) and McCracken et al. (2012). In addition, Marchesi et al. (2016) present a catalogue of 4016 X-ray sources and AGNs in the COSMOS field and measure precise photometric redshifts of these objects; we thus use the photometric redshifts of these X-ray sources from Marchesi et al. (2016). If there are any missing objects and galaxies associated with the extended X-ray emission sources, we determine the overdensity of galaxies using the photometric redshift catalogue presented in Ilbert et al. (2013).

3 IDENTIFICATION OF X-RAY GALAXY GROUPS AND CLUSTERS

The initial catalogues of the COSMOS X-ray groups were published in Finoguenov et al. (2007) and George et al. (2011). These catalogues combined the available *Chandra* and *XMM–Newton* data with developments in the photometric data sets, used for identification of galaxy groups, with confident identification reaching a redshift of 1. They cover mostly massive groups and clusters that are bright in X-rays. For the full details of group identification, we refer readers to Finoguenov et al. (2007), Finoguenov et al. (2009), Finoguenov et al. (2010, 2015), George et al. (2011), and Gozaliasl et al. (2014a).

In this section, we briefly describe the revision of the X-ray centres of the groups using the combined data of *Chandra* and *XMM*, application of the red-sequence finder as a primary procedure for cluster and group identification, and the redshift improvement of galaxy groups relative to their early identification by Finoguenov et al. (2007) and George et al. (2011). Finally, we assign a quality flag to each group based on a visual inspection of the combined X-ray data of the extended sources and the optical RGB images (*i*, *r*, and *g* broad-bands of Suprime-Cam) of galaxies within R_{200} and present the catalogue.

3.1 The revision of the group X-ray centre

Since then, the visionary *Chandra* programme has been completed (Elvis et al. 2009; Civano et al. 2016), providing the high-resolution imaging across the full COSMOS field. In addition, the status of

photometric data provides robust identification of galaxy groups to a much higher redshift. The revised catalogue of extended X-ray sources in COSMOS, released as a part of this paper, is obtained by co-adding all the existing *Chandra* and *XMM–Newton* data in the field. It is very similar to the catalogue used in George et al. (2011), but extends the list of sources beyond the redshift of 1. In addition, we are able to improve on the precision of the centres for extended sources, using the smaller scale emission, detected by *Chandra*, reducing the statistical uncertainty on the centring from 15 arcsec in George et al. (2011) to 5 arcsec. The scales of source confusion are also improved from 32 to 16 arcsec.

Following Finoguenov et al. (2009), in this work we consider the detection using the same spatial scales of 32–128 arcsec as employed in our *XMM* work. On those scales, the combined *Chandra* data add 30 per cent to the existing exposure (or 14 per cent in sensitivity), on average, which results in marginal improvements in the catalogue. The main change, possible with *Chandra* data, is related to the better centring of X-ray emission; as small scales, 16 arcsec scales can also be used. This is of primary importance for the goals of this paper: to separate the BGGs based on the deviation from the X-ray centre. In this work, we increase the sensitivity by using combined *Chandra* + *XMM* data on 16 arcsec scales after rejecting the possibility of point source contamination using *Chandra* data on scales of a few arcseconds, which is sensitive even to three times fainter point sources (Civano et al. 2016). Fig. 1 shows the combined *Chandra* and *XMM–Newton* 0.5–2 keV wavelet-filtered image of the extended X-ray emission sources in the COSMOS field. The emission on scales of 16–256 arcsec is shown. The white contours denote the level of emission at 6×10^{-17}, 3.5×10^{-16}, and 1.2×10^{-15} erg s^{-1} cm^{-2} arcmin^{-2} levels. The emission on scales of 16 arcsec is used to improve the centring. The catalogue of sources corresponds to the signal detected on the 32–128 arcsec scales.
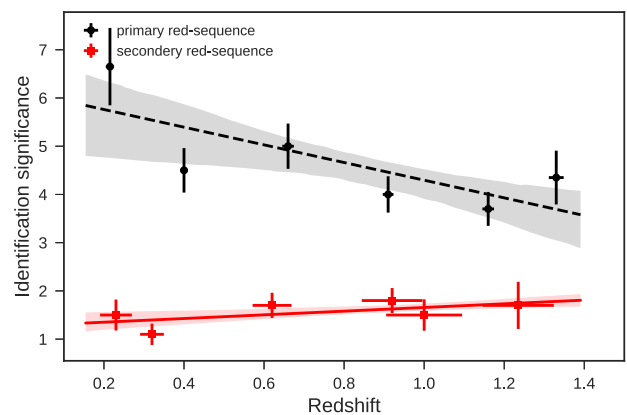
3.2 The red-sequence application

In order to ensure the group and cluster identification, we also use the so-called and refined red-sequence method as described in more detail in Finoguenov et al. (2010, 2015). This is a further refinement of the photo-*z* concentration technique that is used for identification of groups and assigning their redshift (Finoguenov et al. 2007; George et al. 2011).

We run the red-sequence finder for all galaxies located within each extended X-ray emission source. We apply the red-sequence finder to detect any group candidate at a given redshift within different aperture sizes from the X-ray centre/peak of each extended
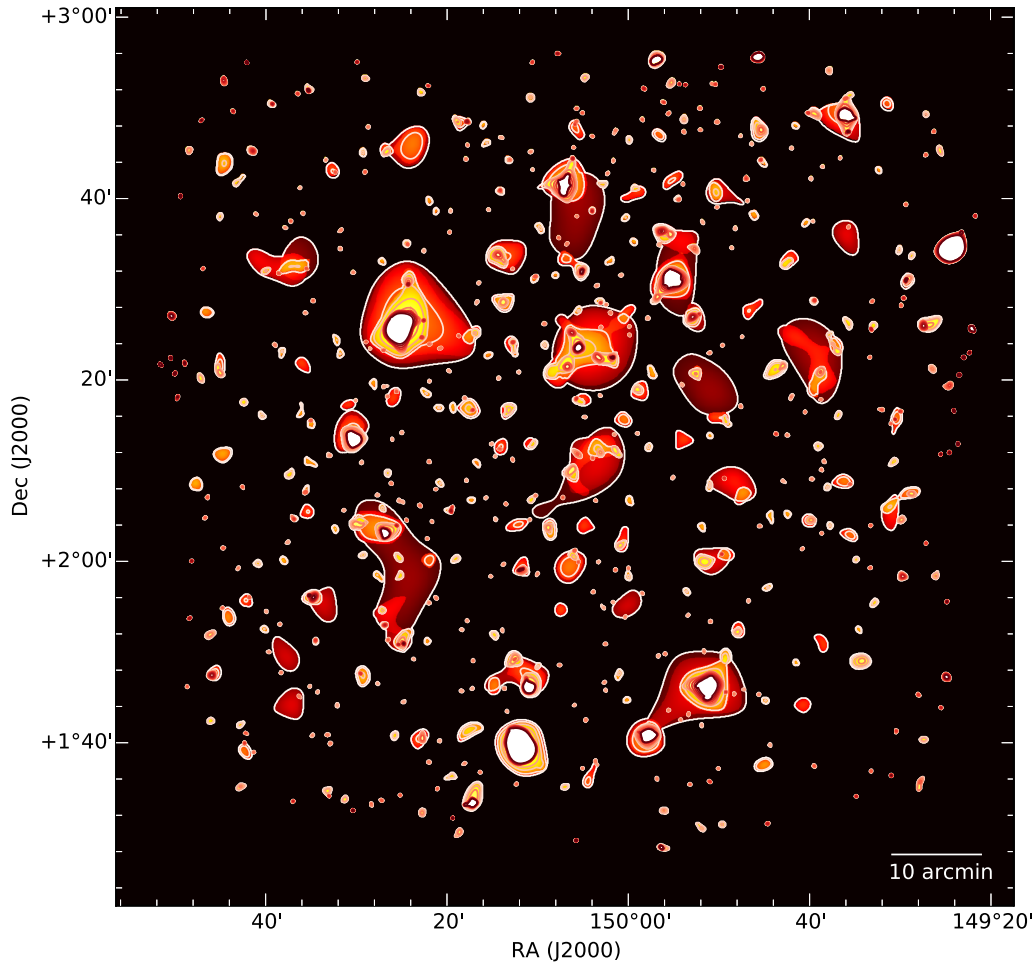
Figure 1. The combined *Chandra* and *XMM–Newton* 0.5–2 keV wavelet-filtered image of the extended X-ray emission in the COSMOS field. The emission on scales of 16–256 arcsec is shown. The white contours denote the level of emission at 6×10^{-17}, 3.5×10^{-16}, and 1.2×10^{-15} erg s^{-1} cm^{-2} arcmin^{-2} levels. The emission on scales of 16 arcsec is used to improve the centring. The catalogue of sources corresponds to the signal detected on the 32–128 arcsec scales. The lowest level of the emission corresponds to real detection only for large-scale sources with areas of 10 square arcmin or more.

X-ray source. The first aperture size that we use to select galaxies for the red-sequence test corresponds to 0.5 Mpc (physical) from the centre of X-ray emission at a given redshift. We also run the red-sequence finder within R_{500} radius of groups that are in common with the Finoguenov et al. ([2007](#)) and George et al. ([2011](#)) catalogues. The application of the red-sequence method can be found in detail in Finoguenov et al. ([2010](#), [2015](#)). As described in these papers, we measure a redshift for any overdensity of red galaxies at the position of a group candidate. To quantify the significance of each red sequence, we assume an aperture of the same size at a random position in the COSMOS field and implement the same procedure 5000 times. We apply a 2σ clipping when estimating the mean/dispersion of redshift. Thus, group regions should be clipped out from the mean/dispersion estimates. This provides us with an average number of red galaxies and their dispersion in the field at a given redshift. The significance of any detected red sequence within an extended X-ray source is evaluated as a relative overdensity of the group candidate to that of the field. Fig. [2](#) compares the median significance of the first (black data points) and second (red data points) solutions (red sequences) versus the redshift. We find that the primary red sequence is always quite significant and more robust than the second red sequence by at least a factor of 2–3 times.

Figure 2. The median of the identification significance versus the redshift of groups when searching for identifying them using the red-sequence method. The black and red data points present the first and second most significant solutions or the primary and secondary red sequences corresponding to each extended X-ray source.
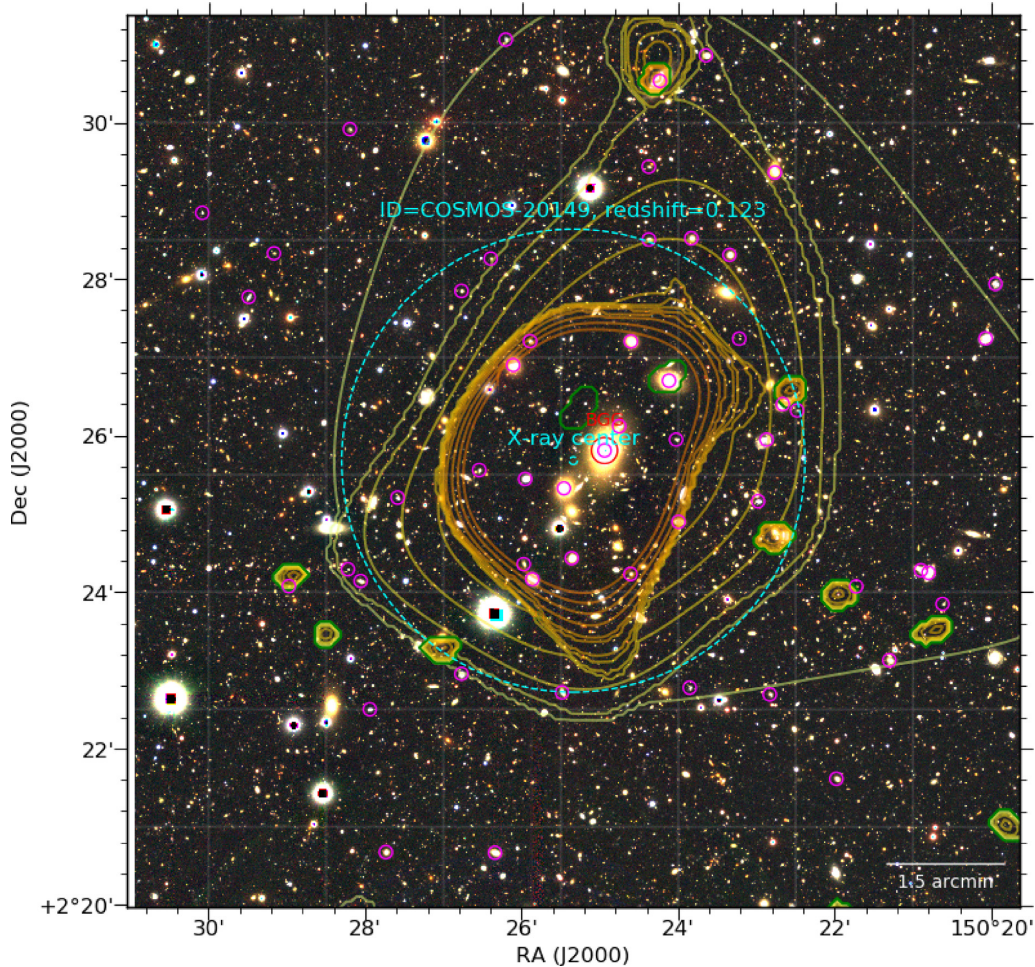
Figure 3. The combined RGB images of *i*, *r*, and *g* bands with overlaid X-ray emission contours (shown in yellow) for group ID 20149 with 50 spectroscopic members (magenta circles). The BGG (red circle) is close to the centre of X-ray peak (small dashed cyan circle). The large dashed cyan circle shows the group's half R_{200}. The small-scale X-ray emission sources (8–16 arcsec) are highlighted with green contours. With this scale, we are able to detect the X-ray emission from the bright group galaxies.

The second red sequence significance is also too low. Fig. 2 also shows that the median significance of the first solution decreases with increasing redshift. We assume the primary red sequence of each extended source and inspect the group candidate by applying the photo-*z*/spec-*z* overdensity technique since the red-sequence method misses star-forming and blue group galaxies.

3.2.1 The redshift determination of groups

Since time that Finoguenov et al. (2007) and George et al. (2011) presented the COSMOS X-ray group catalogues, the COSMOS field has frequently been in the focus of multiband photometric and spectroscopic observations (e.g. McCracken et al. 2012; Le Fèvre et al. 2015; Civano et al. 2016). These observations now provide deep, high-quality multiwavelength data ($AB \sim 25$–26) in the COSMOS field which cover a wide electromagnetic wavelength range from the X-ray to radio bands. The luxury of having precise multi-band photometric redshifts (e.g. Laigle et al. 2016), catalogue of spectroscopic redshifts (M. Salvato et al. in preparation) together with the deep X-ray data of *Chandra* COSMOS-Legacy Survey (Civano et al. 2016; Marchesi et al. 2016) motivated us to revise the previous catalogue of X-ray galaxy groups in the COSMOS field

(Finoguenov et al. 2007; George et al. 2011) and also search for new X-ray groups (Gozaliasl et al. in preparation).

For groups with spectroscopic data available, we update the photometric redshift with a more accurate spectroscopic redshift using the bi-weight location method described in Beers, Flynn & Gebhardt (1990). To avoid the potential contamination due to the presence of substructure, we consider all group members within an R_{500} aperture and obtain an initial group redshift. The proper velocity of each member is then computed and a 3σ clipping is applied to remove any possible projected interlopers. We iterate over multiple steps until the solution converges. Finally, the redshift is assigned if there are three or more spectroscopic members remaining. Groups are visually inspected, especially, where the systems are unrelaxed (i.e. mergers).

Using the bi-weight location method, we estimate the spectroscopic redshift to groups within R_{200} and determine its difference with the redshift estimated using spec-*z* members within R_{500}. Fitting a single Gaussian function to the distribution of $\Delta z (R_{200}, R_{500})$ for groups at $0.04 < z < 1.53$, $0.04 \leq z \leq 0.5$, and $0.5 < z \leq 1.53$, we quantify the dispersion/standard deviation as: $\sigma_{\Delta z} = 0.0038$, 0.0029, and 0.0045, respectively.

In Fig. 3, we show the combined RGB images (*i*, *r*, and *g* filters of the Suprime-Cam of Subaru telescope) with overlaid X-ray contours

for the group ID 20149 at $z = 0.123$. This system includes 50 *spec-z* members within R_{200} (magenta circles). The BGGs are marked with a solid red circle and X-ray peaks as dashed red circles.

All groups and their central galaxies are visually inspected. We find that 143 out of 247 galaxy groups have at least three members with spectroscopic redshifts within R_{500}; the redshift of these galaxies matches the photo-z of groups within errors and this allows the precise assignment of spectroscopic redshifts to these groups. When we increase the aperture size to R_{200}, the number of groups with at least three spectroscopic redshift members increases to 183 out of 247. Thus, the redshift of the 40 out of 247 groups is updated considering their spectroscopic redshift members within R_{200}.

For the rest of the 64 out of 247 groups that contain less than three spectroscopic members, we assign a photometric redshift using the COSMOS2015 catalogue (Laigle et al. 2016), the catalogue of i-selected sources by Ilbert et al. (2008), and the catalogue of X-ray sources (e.g. AGNs) by Marchesi et al. (2016). Further, it is noted that 24 groups (from 64 groups) consist of two spec-z members within R_{200}, which their redshifts match with the group photo-z within errors. In addition, 188/247 central group galaxies in our sample are galaxies with spectroscopic redshifts, which in turn allows us to examine further whether the photo-z of groups is accurate. In summary, we find that 27 and 20 per cent of all group members within R_{500} and R_{200} in our catalogue are spec-z galaxies, respectively.

To revise the redshift of groups with not enough (<3) spec-z members, we measure galaxy overdensities in the photometric redshift space similar to the method used by Finoguenov et al. (2007) and George et al. (2011). We select galaxies from the original photometric redshift catalogue, which have high-quality photometric redshift determination (95 per cent confidence interval) and are not morphologically classified as stellar objects.

The precision of photometric redshift allows us to select redshift slices covering the range $0 < z < 4$. However, for the current catalogue of groups with the majority of them having large-scale X-ray emission, we limit this range to $z < 1.6$. To provide a more refined redshift estimate for the identified structures, we slide the selection window by a 0.05 step in redshift. We add each galaxy as one count and apply the filtering techniques presented by Vikhlinin et al. (1998) to detect excess in the galaxy number density on scales ranging from 20 arcsec to 3 arcmin on a confidence interval of 4σ with respect to the local background. We determine the local background by both the field galaxies located in the same redshift slice and galaxies contributed to the slice due to a catastrophic failure in the photometric redshift.

In order to be sure of the measured photometric redshift of a group, we separately use the Kernel density estimation method (KDE) and determine the redshift distribution and probability density functions (PDFs) for all galaxies associated with each extended X-ray source within $0.5\,R_{200}$. We then determine the redshifts corresponding to the position of the centres of four peaks with high PDFs (>0.4). We then take these redshifts (z_{peak}) and select all galaxies whose redshifts lie at $z_{peak} - z_{err} \leq z \leq z_{peak} + z_{err}$, where z_{err} corresponds to the *photz* precision for the given redshift. For each redshift candidate, we measure the significance of each peak and after a visual inspection, we select the best redshift and update the photometric redshift of the group.

3.2.2 The catalogue description

We describe our catalogue of 247 X-ray galaxy clusters and groups identified so far in the COSMOS field. The full catalogue of galaxy groups is presented electronically. Table 2 lists a sample of these groups with X-ray properties. Column 1 lists the groups and clusters identification ID. The last three digits of this ID present the previous identification ID as defined by Finoguenov et al. (2007) and George et al. (2011). If the X-ray centre of groups is defined based on the small- and large-scale X-ray data, the first digit of the ID begins with 1 and 2, respectively. If the current X-ray centre of previous catalogue needs no correction, the first digit of the ID is 3. Columns 2 and 3 report the right ascension and declination of the position of the peak of the extended X-ray emission from the intra-cluster/intra-group hot gas in equinox J2000.0. Column 4 presents the redshift of clusters and groups.

Column 5 lists group's identification flags. We define four quality flags to describe the reliability of the optical and X-ray counterparts as follows. We assign flag 1, if the group has a secure X-ray emission from the IGM and we can define an X-ray centre. In addition, the group has spectroscopic members in which we are able to measure a spectroscopic redshift for the group. Flag 1 groups generally include central BGGs with spectroscopic redshifts. The group 20149 in Fig. 3 is an example of a Flag 1 group. Flag 2 shows a group that shares the X-ray emission with a foreground/background object and we assign the X-ray flux between them based on the concentration of galaxies and BGG position. In this case, we investigate the X-ray emission from the system using different scales and visually inspect the X-ray contours alignment around the position of the BGG, then define the X-ray centre for the group. In many cases, two groups overlap along the line of sight; the combined data of the *Chandra* and *XMM–Newton* allow us to easily distinguish the distinct X-ray centres. In the lower left panel of Fig. 5, we show two groups at $z = 0.342$ (group 30311) and $z = 0.248$ (group 30224), where X-ray emissions from these systems are overlapping in the line of sight. However, the X-ray resolution allows us to define the X-ray centre independently. Depending on the separation of two sources, we assign Flag 1 or 2 to these sources.

Flag 3 represents a group that has its own specific X-ray centre but with no spectroscopic members and its redshift is defined based on the photometric redshift of galaxies. Flag 4 corresponds to an extended X-ray source with multiple optical counterparts and it is not possible to determine the contribution of each optical counterpart to the observed X-ray emission. In this case, we define the redshift by considering the position of the bright group galaxies and the number of the spectroscopic members. For further detail, we refer the reader to George et al. (2011) and Gozaliasl et al. (2014a).

Column 6 lists group's M_{200} with a $\pm 1\sigma$ error in the ($\times 10^{12}\,M_\odot$) units. M_{200} corresponds to the total mass of groups within R_{200} with respect to the critical density of the Universe. M_{200} is measured using the L_X–M_{200} scaling relation of Leauthaud et al. (2010). Column 7 presents the 0.1–2.5 keV rest-frame X-ray luminosity (L_X) with the error in ($\times 10^{42}\,\mathrm{erg\,s^{-1}}$) within R_{500}. Column 8 reports group R_{200} in degrees, which is estimated using equation (1).

In column 9, we report the IGM temperature with a corresponding $\pm 1\sigma$ error in keV units obtained using the L_x–T scaling relation. Column 10 presents the cluster/group X-ray flux in the 0.5–2 keV band within R_{500} in units of ($\times 10^{-15}\,\mathrm{erg\,cm^{-2}\,s^{-1}}$) with the corresponding $\pm 1\sigma$ errors. Column 11 provides the significance of the X-ray flux estimate that is defined as the ratio of the X-ray flux to its error. Column 12 presents the type of the group redshift: (1) 'spec': we determine groups' *spec-z* using at least three *spec-z* members within R_{500}. (2) 'spec∗': the number of the *spec-z* members of these groups within R_{500} is less than three members; we thus estimate their *spec-z* including *spec-z* members within R_{200}. (3) 'phot': the

Table 2. The revised catalogue of X-ray galaxy groups in 2 deg² of the COSMOS field, which was previously presented by Finoguenov et al. (2007) and George et al. (2011). The full catalogue is available in an online edition.

ID-COSMOS	Ra (J2000)	Dec (J2000)	Redshift(z)	Flag	M_{200c} ($\times 10^{12}\,M_\odot$)	L_X ($\times 10^{42}\,\mathrm{erg\,s^{-1}}$)	R_{200} (deg)	kT (keV)	Flux ($\times 10^{-15}\,\mathrm{erg\,cm^{-2}\,s^{-1}}$)	Flux significance	Redshift type
1006	150.299 51	1.553 43	0.360	1	74.57 ± 4.17	11.53 ± 1.02	0.0425	1.41 ± 0.05	15.96 ± 1.42	11.26	spec
30010	150.750 47	1.531 03	0.669	1	134.42 ± 23.14	43.85 ± 12.35	0.0332	2.32 ± 0.27	14.44 ± 4.07	3.55	spec
20011	150.197 28	1.658 95	0.220	1	170.01 ± 1.73	34.98 ± 0.56	0.0838	2.33 ± 0.02	159.56 ± 2.55	62.58	spec
20017	149.963 75	1.680 22	0.373	1	95.64 ± 4.18	17.21 ± 1.19	0.0453	1.66 ± 0.05	22.69 ± 1.57	14.46	spec
30018	149.765 18	1.623 55	0.371	2	33.44 ± 6.68	3.33 ± 1.10	0.032	0.87 ± 0.10	4.33 ± 1.43	3.04	spec
20020	150.325 84	1.605 10	0.227	2	21.19 ± 2.62	1.35 ± 0.27	0.0419	0.65 ± 0.04	6.16 ± 1.23	5.01	spec
20023	150.380 68	1.675 76	0.701	1	51.63 ± 5.79	10.30 ± 1.86	0.0233	1.25 ± 0.09	2.63 ± 0.48	5.53	spec
20024	150.291 69	1.689 35	0.527	1	49.85 ± 4.31	7.65 ± 1.06	0.0281	1.16 ± 0.06	4.10 ± 0.57	7.22	spec
20025	149.854 02	1.770 23	0.124	1	44.33 ± 0.88	3.84 ± 0.12	0.0884	0.96 ± 0.01	63.14 ± 1.98	31.94	spec
20029	150.181 67	1.770 86	0.344	1	64.47 ± 2.41	8.96 ± 0.53	0.0422	1.28 ± 0.03	14.09 ± 0.83	16.91	spec
10031	150.492 37	1.794 25	0.958	2	66.28 ± 8.04	21.82 ± 4.27	0.0207	1.61 ± 0.13	2.51 ± 0.49	5.11	spec
20035	150.210 20	1.820 14	0.529	1	47.09 ± 4.38	7.02 ± 1.05	0.0275	1.12 ± 0.06	3.69 ± 0.55	6.71	spec
20039	149.821 26	1.825 43	0.531	1	39.97 ± 4.58	5.44 ± 1.01	0.0260	1.01 ± 0.07	2.83 ± 0.52	5.42	spec
10040	150.412 50	1.848 88	0.973	1	82.31 ± 6.07	31.08 ± 3.65	0.0221	1.86 ± 0.09	3.67 ± 0.43	8.51	spec
20052	150.447 59	1.883 19	0.672	1	41.22 ± 5.44	6.93 ± 1.48	0.0223	1.08 ± 0.09	1.93 ± 0.41	4.68	spec
20054	150.586 64	1.937 61	0.310	2	40.07 ± 3.36	4.08 ± 0.55	0.0392	0.95 ± 0.05	8.32 ± 1.12	7.46	spec
20058	150.123 93	1.911 44	0.736	1	35.10 ± 7.19	5.91 ± 2.00	0.0199	1.00 ± 0.12	1.24 ± 0.42	2.96	spec
20064	150.198 21	1.985 06	0.440	1	32.05 ± 3.24	3.41 ± 0.55	0.0278	0.87 ± 0.05	2.88 ± 0.47	6.16	spec
20065	149.892 53	1.944 59	0.773	1	28.96 ± 6.99	4.61 ± 1.85	0.0181	0.91 ± 0.12	0.78 ± 0.31	2.49	spec
20067	149.744 10	1.952 29	0.483	5	26.80 ± 5.06	2.69 ± 0.83	0.0248	0.79 ± 0.08	1.86 ± 0.58	3.22	spec
20068	149.999 60	1.973 28	0.600	1	32.52 ± 5.31	4.34 ± 1.16	0.0223	0.92 ± 0.09	1.59 ± 0.42	3.75	spec
20069	150.419 65	1.973 82	0.863	1	29.82 ± 9.86	5.48 ± 3.08	0.0170	0.95 ± 0.18	0.64 ± 0.36	1.78	spec
20071	150.365 66	2.002 52	0.828	1	53.59 ± 6.25	13.05 ± 2.45	0.0212	1.34 ± 0.10	2.13 ± 0.40	5.32	spec
10073	150.091 86	1.999 08	0.221	1	18.52 ± 1.64	1.10 ± 0.16	0.0397	0.61 ± 0.03	4.86 ± 0.69	7.06	spec
10041	149.9323	1.830 45	0.530	2	24.82 ± 5.03	2.582 ± 0.86	0.0222	0.77 ± 0.08	1.28 ± 0.43	2.99	spec*
10105	150.382 95	2.102 78	1.163	1	61.21 ± 10.48	25.61 ± 7.17	0.0179	1.64 ± 0.18	1.64 ± 0.46	3.57	phot

Note: Column 1 lists identification ID. Columns 2 and 3 present right ascension and declination of the X-ray peak (centre) in equinox *J2000.0*. Columns 4 and 5 present the redshift and group's identification flags. Columns 6 and 7 list M_{200} with a $\pm 1\sigma$ error in ($\times 10^{12}\,M_\odot$) and the X-ray luminosity (L_X) with a corresponding $\pm 1\sigma$ error in ($\times 10^{42}\,\mathrm{erg\,s^{-1}}$) within r_{500}. Column 8 reports group R_{200} in degree. Columns 9 and 10 report the IGM temperature (kT) with a corresponding $\pm 1\sigma$ error in keV and the X-ray flux in the 0.5–2 keV band within r_{500} in ($\times 10^{-15}\,\mathrm{erg\,cm^{-2}\,s^{-1}}$) with $\pm 1\sigma$ errors. Column 11 provides the significance of the X-ray flux estimate. Column 12 presents two types of the assigned redshifts to the groups: *spec-z*, and *phot-z*. The redshifts of groups with the *'spec∗-z'* are measured using their *spec-z* members within R_{200}. The redshifts of the rest of groups with *'spec-z'* are determined using their *spec-z* members within R_{500}. We note that the errors are presented in separate columns in the electronic version of the catalogue.
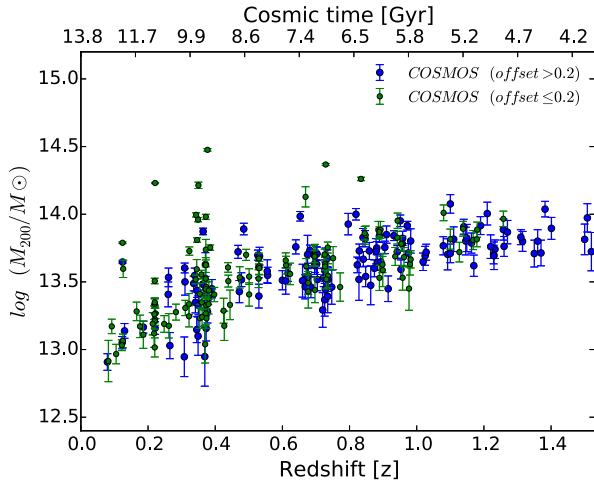
Figure 4. The halo mass of X-ray galaxy groups (M_{200}) within R_{200} (defined as the radius delimiting a sphere with an interior mean density 200 times the critical density) as a function of redshift. Each colour of data points represents a sample of groups that have been selected based on the ratio of the offset of the BGG position from the X-ray centre of haloes to the R_{200} radius.

redshifts of these groups are determined using the photometric redshift of group galaxies.

4 SAMPLE DEFINITION AND DATA

4.1 Sample definition

In this section, we describe the BGG selection and the definition of subsamples. We make use of our revised catalogue of 247 X-ray galaxy groups with $M_h \sim 5 \times 10^{12}$ to $10^{14.5}$ M$_\odot$ at $0.08 < z < 1.53$, detected from the COSMOS field. Fig. 4 presents the halo mass of groups as a function of their redshifts. The halo mass (M_h) corresponds to the total mass of groups as

$$M_\Delta = \frac{4\pi}{3}\Delta \times \rho_{crit} \times R_\Delta^3, \qquad (1)$$

where ρ_{crit} is the critical density of the Universe and R_Δ is defined as the radius delimiting a sphere whose interior mean density is Δ times the critical density of the Universe at the group and cluster redshift. Several choices of Δ are in use in different studies, from an overdensity of 180, 200, and 500 times the mean/critical density of the matter in the Universe (Diaferio et al. 2001; Kravtsov et al. 2004).

N-body simulations suggest that clusters and groups are expected to be virialized within overdensities with $\Delta \sim 200$ times the critical/mean density of the matter in the Universe (Cole & Lacey 1996). $R_{\Delta = 200}$ (hereafter R_{200}) is generally used as the characteristic radius to determine cluster/group membership and corresponding physical properties of haloes. In this study, we select group members and BGGs (the most massive and luminous group members) within R_{200} (e.g. Lin & Mohr 2004).

The halo mass of groups in this study corresponds to the total mass of groups (M_{200}) within R_{200}. We determine M_{200} using the scaling relation of L_X–M_{200} with weak lensing mass calibration as presented by Leauthaud et al. (2010). The L_X–M_{200} scaling relation of the COSMOS galaxy groups and similar data sets have been already extensively studied, and full details of this relation and the

Table 3. The average systematic error (se) and the statistical error on the mean (sem) of $\log(M_\star/\mathrm{M}_\odot)$ and $\log(M_{200}/\mathrm{M}_\odot)$ for S-I to S-V. The error values are in dex.

Sample	$M_\star$ (se)	$M_\star$ (sem)	M_{200} (se)	M_{200} (sem)
S-I	0.12	0.08	0.16	0.01
S-II	0.15	0.07	0.12	0.02
S-III	0.16	0.07	0.15	0.01
S-IV	0.15	0.05	0.15	0.01
S-V	0.19	0.05	0.16	0.02

L_X–σ and M_X–M_{dyn} relations can be found in studies by Leauthaud et al. (2010), Connelly et al. (2012), Erfanianfar et al. (2013), and Kettula et al. (2015). Note that we include a 0.08 dex extra error in halo mass estimate, which corresponds to log-normal scatter in the L_x–M_{200} relation (Allevato et al. 2012). We also study the scaling relations of our sample of *spec-z* groups in Gozaliasl et al. (in preparation).

Fig. 4 presents the halo mass of groups (M_{200}) within R_{200} (defined as the radius delimiting a sphere with an interior mean density 200 times the critical density) as a function of redshift. As can be seen, a large fraction of the groups have a halo mass range of $13.50 < \log(\frac{M_{200}}{\mathrm{M}_\odot}) \leq 14.02$.

This mass regime exactly corresponds to a transition zone from massive clusters to low-mass groups, which is the main point of interest in this study. Following Gozaliasl et al. (2016, 2018), we select five subsamples of galaxy groups according to the halo mass and redshift plane as

(S-I) $0.04 < z < 0.40$ and $12.85 < \log(\frac{M_{200}}{\mathrm{M}_\odot}) \leq 13.50$
(S-II) $0.10 < z \leq 0.40$ and $13.50 < \log(\frac{M_{200}}{\mathrm{M}_\odot}) \leq 14.02$
(S-III) $0.40 < z \leq 0.70$ and $13.50 < \log(\frac{M_{200}}{\mathrm{M}_\odot}) \leq 14.02$
(S-IV) $0.70 < z \leq 1.00$ and $13.50 < \log(\frac{M_{200}}{\mathrm{M}_\odot}) \leq 14.02$
(S-V) $1.00 < z \leq 1.30$ and $13.50 < \log(\frac{M_{200}}{\mathrm{M}_\odot}) \leq 14.02$.

The subsamples from S-II to S-V have the same halo mass range but they are at different redshift ranges. This allows us to compare the stellar mass distribution of galaxies within haloes of the same mass at different redshifts. On the other hand, S-I and S-II have similar redshift ranges but different halo mass ranges. This enables us to explore the impact of halo mass on the BGG mass distribution over $z < 0.4$. In Table 3, we report the mean statistical and systematic errors in the halo mass of groups and the stellar mass of BGGs in each subsample.

4.2 The semi-analytic models

We interpret our results using two SAMs by Guo et al. (2011, hereafter G11) and Henriques et al. (2015, hereafter H15). Both models are based on merger trees from the Millennium Simulation (Springel et al. 2005) that provides a description of the evolution of the distribution of dark matter structures in a cosmological volume. While G11 use the simulation in its original WMAP1 cosmology, H15 scale the merger trees to follow the evolution of LSSs expressed for the more recent cosmological measurements and Planck results. With respect to the treatment of baryonic physics, G11 and H15 follow the Munich model, L-Galaxies. A summary of the properties of these SAMs can be found in Gozaliasl et al. (2014a, 2018) and for their full details, we refer readers to Guo et al. (2011), Henriques et al. (2013), and Henriques et al. (2015).

Both SAMs of H15 and G11 define a parameter known as 'type' with different values (0, 1, and 2) to select central/satellite galaxies. Type = 0 if a galaxy is at the centre of the friend-of-friend (FOF) group, type = 1 if the galaxy is at centre of the subhalo but not at the centre of its FOF group, finally, if a galaxy is a satellite that has lost its subhalo then its type is 2. We select BGGs in models similar to that in observations and assume them to be the most massive galaxies within the R_{200} of the FOF group.

In this study, we use the data from the H15 and G11 SAMs and randomly select 5000 BGGs within haloes with the halo mass and redshift ranges as described for S-I to S-V and compare the model predictions with our observational results in Sections 5.2 and 5.3.

4.3 The hydrodynamical simulation of magnetium

For the comparison with hydrodynamical simulations, we use galaxies and galaxy clusters selected from the Magneticum Pathfinder (www.magneticum.org) simulation set, which adopts a WMAP7 (Komatsu et al. 2011) ΛCDM cosmology with $\sigma_8 = 0.809$, $h = 0.704$, $\Omega_m = 0.728$, $\Omega_\Lambda = 0.272$, $\Omega_b = 0.0456$, and an initial slope for the power spectrum of $n_s = 0.963$. This suite of fully hydrodynamic cosmological simulations comprises a broad range of simulated volumes, where for our purpose we choose the *Box2/hr* that uses 2×1584^3 particles to simulate a cosmological volume of $(500 \text{ Mpc})^3$. In this simulation, the stellar component is represented by stellar sink particles with a mass of $m_* = 3.5 \times 10^7 \text{ M}_\odot$ and a gravitational softening of $\epsilon_* = 2.0 \, h^{-1}$ kpc.

All simulations of the Magneticum Pathfinder simulation suite are performed with an advanced version of the tree-SPH code P-GADGET3 (Springel et al. 2005). They include metal-dependent radiative cooling, heating from a uniform time-dependent ultraviolet background, star formation according to Springel & Hernquist (2003), and the chemo-energetic evolution of the stellar population as traced by SN Ia, SN II, and AGB stars, including the associated feedback from these stars (Tornatore et al. 2007). Additionally, they follow the formation and evolution of supermassive black holes, including their associated quasar and radio-mode feedback. For a detailed description, e.g. see Dolag et al. (in preparation), Hirschmann et al. (2014), and Teklu et al. (2015).

We use the SUBFIND algorithm (Springel et al. 2001; Dolag et al. 2009) to define halo and subhalo properties. SUBFIND identifies substructures as locally overdense, gravitationally bound groups of particles that can be associated with galaxies. This implies that the stellar mass of the main galaxy within a galaxy cluster or group always represents not only the BCG but also the intra-cluster light (ICL) component. The predicted stellar mass function of the simulations generally compares well with the observed one over a large range of redshift intervals (see Gozaliasl et al. in preparation). Despite this reasonably good agreement, the simulations predicted that stellar masses of BCGs are significantly larger than the observed ones. This can be partially a sign of there being still not efficient enough AGN feedback in the simulations, but also can be caused by the fact that the stellar mass estimates from the BCGs in the simulations also account for the ICL. Distinguishing between the BCG and ICL is a notoriously difficult task. Based on a dynamical separation of these two stellar components, simulations indicate that the stellar mass associated with the BCG is only ≈45 per cent of the total, BCG + ICL mass, see Dolag, Murante & Borgani (2010) and Remus, Dolag & Hoffmann (2017). However, it is observationally significant that some fraction of the ICL will contribute to the observed light from the BCG and therefore the observed fraction will be larger and depends on the magnitude cut used (see Cui et al.

2013). Therefore, we assume that the observed stellar mass fraction of the simulated BCG would generally correspond to 70 per cent of the mass of the total stellar mass (BCG + ICL) inferred from the simulations.

4.4 The BGG selection

In this study, the BGG is defined as: (i) the most massive galaxy, (ii) within R_{200} of the group X-ray centroid, (iii) with a redshift that agrees with that of the hosting group as estimated from all the redshifts available around the X-ray centroid.

For selecting BGGs, a different choice of apertures from the group X-ray centroids is examined. As mentioned above, we also examine different choices of the BGG selection within a variety of group radii and apertures from the group X-ray centroids (R_{200}, R_{500}, and $0.5R_{500}$). We find that when selecting BGGs within $0.5R_{500}$, a number of low-mass galaxies are selected as BGGs while there are more massive galaxies at about ∼100–300 kpc from these galaxies. The differences between the BGG selections within R_{200} and R_{500} are not meaningful. For this study, we select BGGs within R_{200}, while we show the stellar mass distribution for all BGGs selected within three different radii in Section 4.1.

Altogether 188 BGGs are selected using their spectroscopic redshifts and 59 BGGs in our sample are selected using the photometric redshifts considering a $\pm 0.007(1 + z)$ photo-z accuracy (McCracken et al. 2012; Ilbert et al. 2013; Laigle et al. 2016). All BGGs are visually inspected using the RGB image of hosting groups including the overlaid extended X-ray emission contours (see Fig. 5).

### 4.5 The BGG offset from halo X-ray centre

4.5.1 Definition of the BGG offset

The majority of the brightest cluster galaxies (BCGs) mostly lie at the bottom of the potential well of the host cluster and their X-ray peaks/centres with no considerable offsets (e.g. Jones & Forman 1984; Postman & Lauer 1995; Lin & Mohr 2004; Lavoie et al. 2016). It is still unknown whether environments act on galaxy evolution when transiting from a massive cluster-regime to a low-mass group-regime. Are BGGs located at the centre of hosting haloes and do they evolve in the same way as BCGs? The multiband data and our well-controlled statistical sample of X-ray groups enable us to answer this question and explore the evolution of BGGs in the galaxy cluster-group transition regime ($M_h \sim 10^{13-14} \text{ M}_\odot$) out to the elusive high redshift of $z = 1.5$.

It is well recognized that the dynamical state of groups differs significantly from that of clusters. Groups are likely located where the velocity dispersion of galaxies is sufficiently low, which allows merging and interaction between galaxies to happen frequently, and thus groups can evolve significantly in a fraction of Hubble time.

N-body modelling experiments have shown that a fraction of current-epoch groups, even those with apparently short dynamical times ($\sim 0.1 \, H_0^{-1}$), are probably relatively young systems that might only just been collapsed and they will possibly undergo significant dynamical evolution (Barnes 1985).

On the other hand, according to the ΛCDM model, groups are the building blocks of massive structures in the universe and they are accreted by massive clusters. Those groups undergo major mergers and halo mergers, BGGs might be far from the minimum of the potential wells and they could lie far from the X-ray centres (peaks).
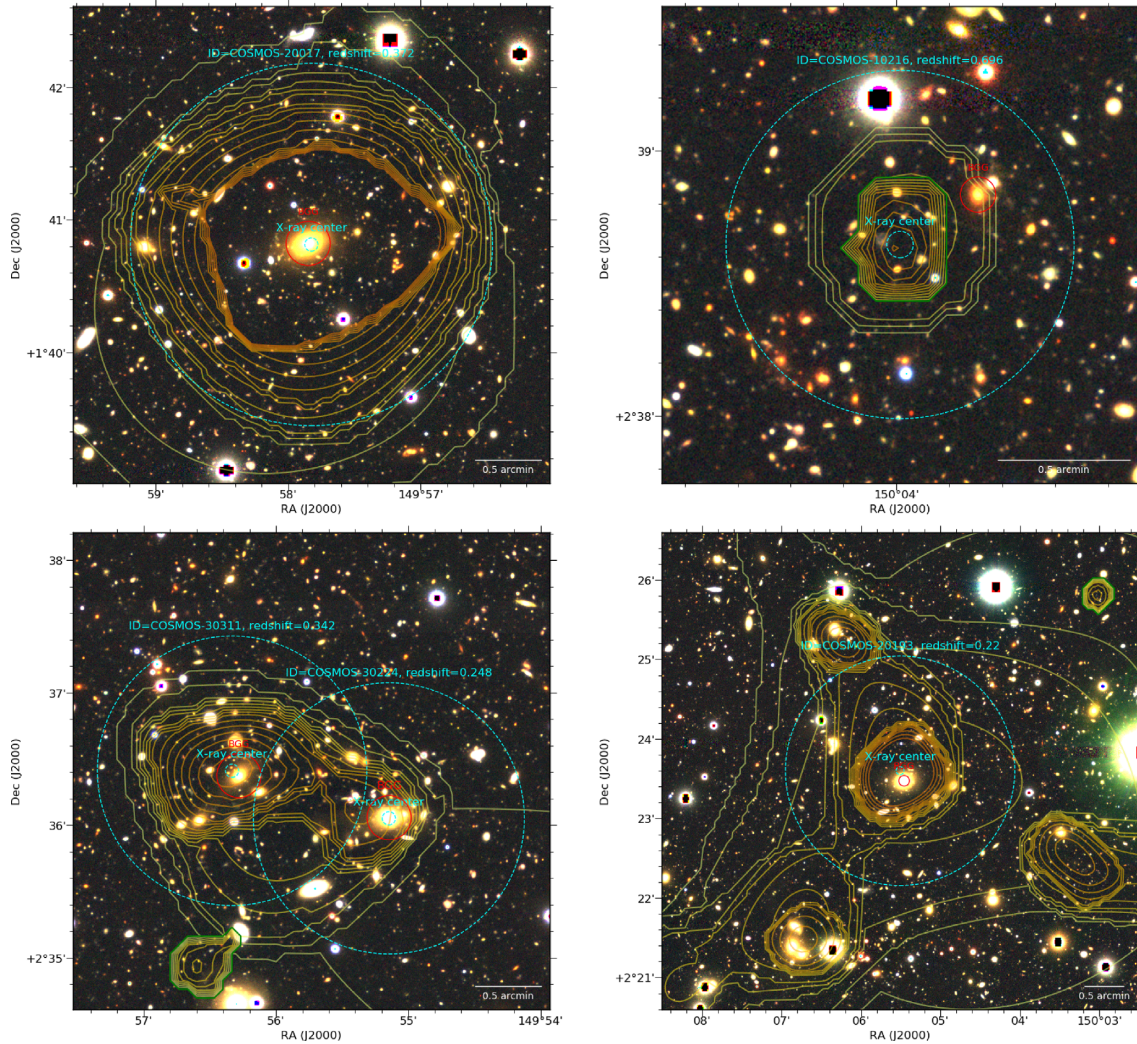
Figure 5. The combined RGB optical images of *i*, *r*, and *g* Subaru broad-bands of four X-ray galaxy groups in COSMOS. The combined *Chandra* and *XMM* X-ray emission contours are shown in yellow. Group X-ray centre/peak and $0.5R_{200}$ radius are illustrated with dashed small and large cyan circles, respectively. The BGG is marked with a red circle in each group. *Upper left panel*: an example of a centrally dominant BGG with no offset from the X-ray centre of a flag = 1 group at $z = 0.372$. *Upper right panel*: an example of a BGG with a large offset from the X-ray centre of a flag = 1 group at $z = 0.696$. *Lower left panel*: an example of two BGGs with no offset from the X-ray centres of two groups at $z = 0.342$ and 0.248, which their extended X-ray emissions are projected. However, the combined X-ray data of *Chandra* and *XMM* allow us to assign an X-ray centre to each group correctly. *Lower right panel*: an example of a BGG with no offset from the group X-ray centre of a group at $z = 0.220$. The X-ray contours show three subhaloes that belong to the parent halo at the centre of the image.

If this scenario is true, we expect that a fraction of BGGs may offset from the group X-ray peaks even at distances larger than 0.5 R_{500}. The BCGs are mostly selected within a small distance to the cluster X-ray centres (see Lavoie et al. 2016; Harvey et al. 2017; Trevisan & Mamon 2017; Golden-Marx & Miller 2018; Lopes et al. 2018). In this study, we investigated the BGG offset with respect to three different group radii: $0.5R_{500}$, R_{500}, and R_{200}. Therefore, the offset of BGGs is defined as the ratio of their angular separations from the halo X-ray centroid (r) to the given group's radius (e.g. here R_{200}) as

$$\text{offset} = \frac{r}{R_{200}}. \qquad (2)$$

We select a clean sample of the observed groups (flag ≤ 3) and BGGs in COSMOS where we are able to assign an X-ray centre for each group and study the BGG offset with excluding groups with low identification and X-ray flux significance.

Based on the BGG offset from the X-ray centroids, we classify them into the following three classes in each subsample (S-I to S-V):

(i) Central dominant BGGs with an offset ≤ 0.2,
(ii) Large-offset BGGs with an offset > 0.2, and
(iii) All BGGs with any offset ≤ 1.

In Fig. 4, we illustrate haloes having BGGs with low and large offsets with filled green and blue circles, respectively. In the upper panel of Fig. 5, we also show two examples of the central dominant BGG (left-hand panel) and BGG with a large offset (right-hand panel).

In the following subsection, we investigate the distribution and evolution of the BGG offset and its relations with the halo mass, X-ray flux, the significance of the X-ray flux, and *r*-band magnitude gap between two BGGs.

4.5.2 Distribution of the BGG offset

The upper left panel of Fig. 6 shows the cumulative distribution of the projected distance from the X-ray peak for the full sample of BGGs (black dot line) and BGGs for S-I to S-V. We see that ~80 per cent of all BGGs (black line) have an offset $\leq 0.5R_{200}$. We are aware that the adoption of a large radius (R_{200}) could result in a larger background/foreground contamination in selecting BGGs. This is a major problem if there is no complete spectroscopic coverage. We also consider that for merging systems R_{200} could be overestimated, implying a BCG selection within an unnecessarily large radius. To avoid these uncertainties, we first exclude groups with low identification significance applying the flag ≤ 3 limit, visual inspection of the group's image, and then examine the BGG selection within smaller radii ($0.5R_{500}$, R_{500}). In addition, our groups are mostly spec-z systems with spec-z BGGs. Finally, we find that it is true that adopting smaller radii may decrease the background/foreground contamination, however, it causes that in some groups very low-mass centrally located satellite galaxies with $M_* < 10^9$ $M_\odot$ are selected as BGGs, while the true BGGs lie with offset from the group X-ray centroid. We investigate this in more details in Section 5.1.

We suggest that for a sample of photo-z groups with not enough spec-z using a smaller radius like $0.5R_{200}$ to select BGGs could be a confident approach, so that you can choose the true BGGs, not risking background/foreground contamination at larger radius.

We apply the K–S test and quantify p-value and the differences between the cumulative distributions of the BGG offset for S-II ($z = 0.1$–0.4) and S-V ($z = 1.0$–1.3). The p-value corresponds to ~0.06 and we are not able to reject the null hypothesis that the two samples were drawn from the same distribution. There is also a $D = 0.36$ difference between two distributions at $r/R_{200} = 0.2$. As a result, we suggest that BGGs are likely to become central galaxies with decreasing redshifts and their offsets widen at higher redshifts.

4.5.3 Evolution of the BGG offset

The upper right panel of Fig. 6 presents the median value of the BGG offset from the X-ray centre as a function of the redshift of the host groups. We note that the trend of the r/R_{200}–z relation does not change significantly when we exclude the BGGs for S-I from the data and plot this relation for S-II to S-V. This redshift evolution of the BGG offset is evident here and we quantify the relation between the BGG offset (r/R_{200}) and redshift (z) as

$$r/R_{200} = (0.174 \pm 0.002) + (0.167 \pm 0.003) \times z \, ; \qquad (3)$$

we find that the BGG offset (r/R_{200}) evolves as a function of redshift and it decreases by ~0.25 from $z = 1.53$ to the present day.

4.5.4 The relation between the BGG offset and halo mass

We show the median value of the BGG offset as a function of the group's M_{200c} in the middle left panel of Fig. 6. The BGG offsets are plotted as a function of the group's critical halo mass $\log(M_{200c}/M_\odot)$ for the given three redshift bins, $z = 0.0$–0.5 (solid black line and filled circles), $z = 0.5$–1.0 (dashed blue line and filled squares), and $z = 1.0$–1.5 (dotted red line and filled diamonds), individually. We find that the BGG offset decreases with increasing halo mass as the slope of the relation negatively increases as a function of increasing redshift. The slope of this relation for each redshift bin, $z = 0.0$–0.5, 0.5–1.0, and 1.0–1.5, is quantified using the linear regression

model as -0.116 ± 0.002, -0.273 ± 0.04, and -0.922 ± 0.188, respectively.

### 4.5.5 The relation between the BGG offset and the group X-ray flux

As discussed above, the BGG offsets widen towards higher-z. This could be due to lower fluxes and SNR ratios or as a result of a group evolution. Hence, to address how much of the effect could be driven by noise, we inspect the relationship between the median value of the BGG offset and the group's X-ray flux (see the middle right panel of Fig. 6) at three redshift bins, $z = 0.0$–0.5 (solid black line and filled circles), $z = 0.5$–1.0 (dashed blue line and filled squares), and $z = 1.0$–1.5 (dotted red line and filled diamonds), respectively. It appears that the data show a weak negative correlation between the BGG offset and the group's X-ray flux at $z = 0.0$–0.5 while there is no correlation at high redshifts. This finding is also more evident in the lowest panel of Fig. 6 where we present the relation between the offset of the majority of our BGGs sample and their host groups' flux significances (<10). We define the flux significance as the ratio of the flux to flux error. In this panel, we also show a two-dimensional histogram that counts BGGs within given offset and flux significance bins. We find that there is no preferential trend between offset and flux significance and the BGG offset spreads a wide dynamic range at any given flux significance. This means that the offsets of BGGs from the X-ray centroids are not driven by observational noise.

We note that there are 15 additional systems with higher flux significance (10–62) outside the plot range. These systems are the most massive groups and clusters in our sample and hence have very bright X-ray significances. Their BGG/BCG offsets range from ~0 to 0.4.

4.5.6 The relation between the BGG offset and magnitude gap

The difference between the first and second ranked galaxy magnitudes in groups is often considered a tracer of their merger histories and dynamical evolution (Barnes 1989; Ponman et al. 1994; Gozaliasl et al. 2014a; Khosroshahi et al. 2014; Raouf et al. 2014; Trevisan & Mamon 2017). Using N-body simulations of isolated groups, various studies found early on that galaxy mergers in groups will lead to the runaway growth of the most massive central galaxy (Carnevali, Cavaliere & Santangelo 1981; Cavaliere et al. 1986; Barnes 1989; Mamon 1992).

This growth may occur independently of the merger mechanism (Mamon 1987), whether the group evolves through direct merging between galaxies or due to orbital decay via dynamical friction that causes group galaxies to lose energy and angular momentum against a diffuse background. In both hypotheses, the growth of the BGG happens at the expense of the second brightest group galaxy (SBGG), because the merger cross-section for SBGG is greater than that of the less massive and luminous satellites; in addition, the dynamical friction time scales as the inverse of the galaxy subhalo mass, leading to faster orbital decay of the SBGG (Chandrasekhar 1943), hence more rapid merging with the BGG. According to this scenario, as a group evolves through merging, the magnitude gap should also grow in time. The final product of such a rapid growth of the central group galaxy is a group that includes a giant elliptical galaxy surrounded with some faint satellites with a luminous X-ray halo (bolometric $L_X > 10^{42} \, h_{50}^{-2}$ erg s^{-1}), exhibiting a large magnitude gap ($\Delta M_{1,2} > 2$) with the second SBGG within $0.5R_{200}$ (Jones
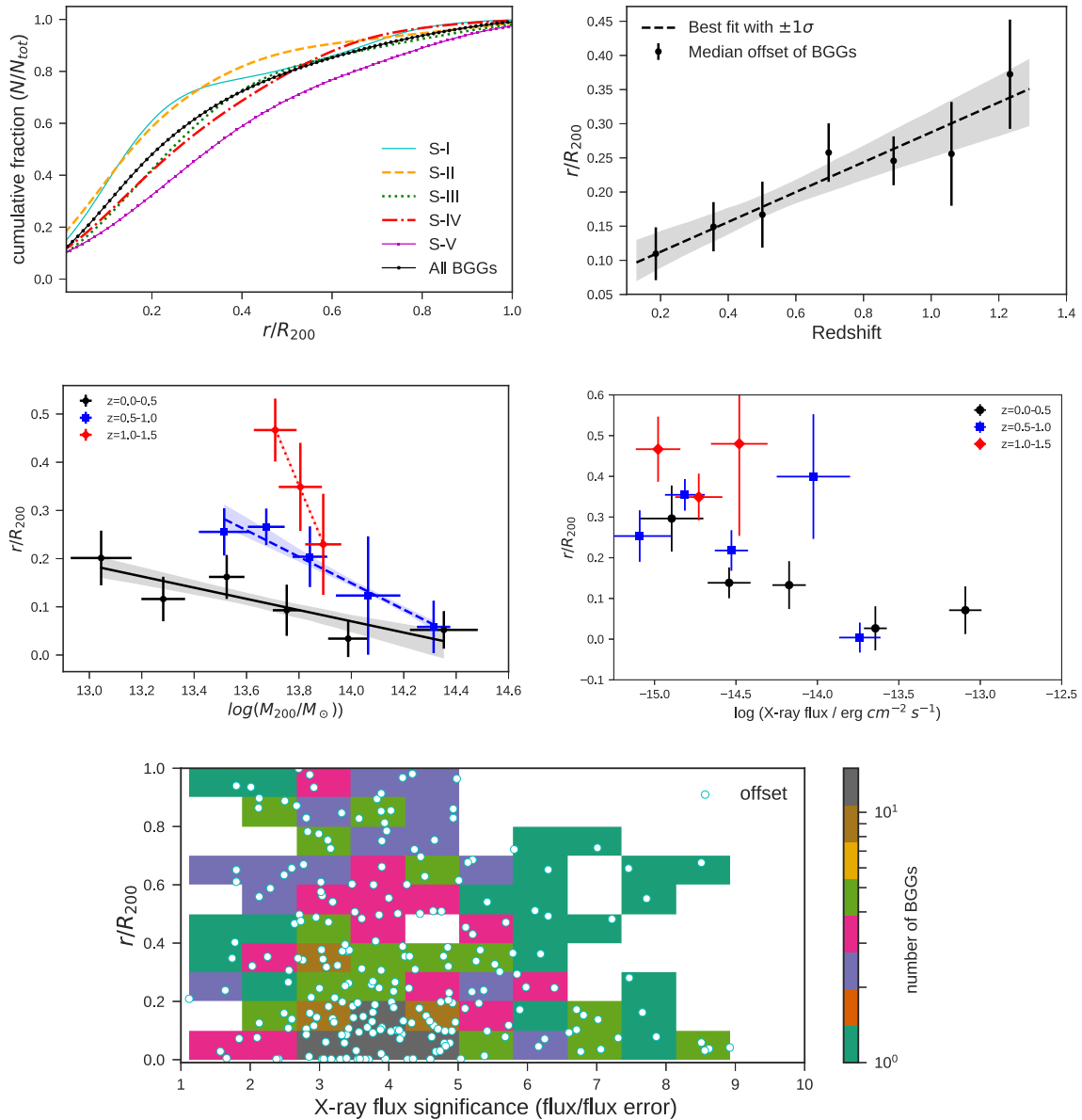
Figure 6. *Upper left panel:* Cumulative distribution of the projected radial offset of the BGGs from the X-ray centre for S-I to S-V and the full sample of BGGs (solid black line with filled circles). The distance of the BGG from the X-ray centre (r) is normalized to the radius of each group, R_{200}. The number of galaxies located within a given distance is normalized to the total number of BGGs within each subsample. *Upper right panel:* The redshift evolution of the median values of the offset of the full sample of BGGs from the X-ray centre of hosting groups. The BGG offset from the X-ray centre decreases as a function of the redshift by a factor of 3 since $z = 1.3$ to present day. *Middle left and right panels:* The BGG offset (r/R_{200}) as a function of the group's halo mass (M_{200c}) (left) and the group X-ray flux (right) for BGGs at $z = 0.0$–0.5 (solid black line and filled circles), $z = 0.5$–1.0 (dashed blue lines and filled squares), and $z = 1.0$–1.5 (dotted red line and filled diamonds), respectively. The BGG offset decreases as a function of increasing halo mass and the slope of this relation increases interestingly with increasing redshift. *Lower panel:* The BGG offset (r/R_{200}) as a function of the flux significance (flux/fluxer). The colour bar presents the number of BGGs within given offset and the flux significance bins.

et al. 2003). These types of groups are known as 'fossil groups' and the first fossil group was discovered by Ponman et al. (1994).

Fossils are early formed and relaxed systems (Gozaliasl et al. 2014b), as a result, the BGGs in fossils are central dominant galaxies with the lowest offset from the group X-ray-centroid halo. We investigate here the relation between the BGG offset from the X-ray centre and the magnitude gap between two BGGs.

Recently, Lopes et al. (2018) used two samples of the Sunyaev–Zel'dovich (SZ) and X-ray-selected galaxy clusters ($z < 0.11$) and estimated the dynamical state of clusters using the BCG-X-ray cen-

troid offset, and the magnitude gap between the first and second BCGs. They recommend an offset cut-off $\sim 0.01 \times R_{500}$ to separate relaxed and disturbed clusters. Regarding the magnitude gap, the separation can be done at $\Delta m_{1,2} = 1.0$. They showed that 20 and 60 per cent of the relaxed and disrupted clusters include BCGs with large offsets.

Trevisan & Mamon (2017) studied the magnitude gap and the conditional luminosity function of the SDSS groups (Yang et al. 2007) and found that some groups, preferentially small-gap groups, have more than one central galaxy.
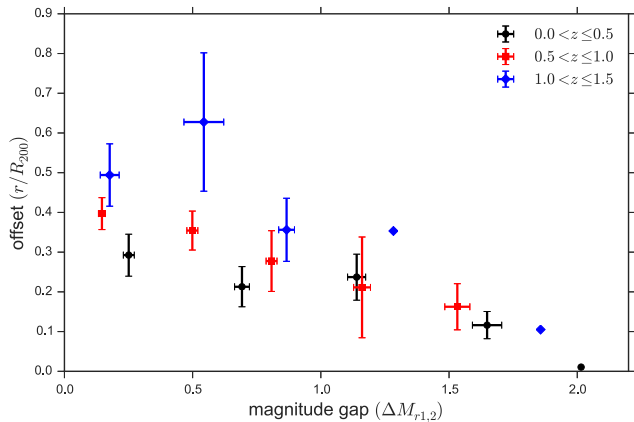
Figure 7. The relation between the BGG offset from the group X-ray peak/centre and the r-band magnitude gap ($\Delta M_{1,2}$) between the first and second brightest group galaxies within R_{200} at $z = 0.0$–0.5 (black circles), $z = 0.5$–1.0 (red squares), and $z = 1.0$–1.5 (blue diamonds). The BGG offset from the X-ray centre of groups shows a negative correlation with the magnitude gap with no redshift-dependent trend. Groups with a large magnitude gap (e.g. fossils) represent BGGs with the lowest offset from the halo X-ray centre.

Golden-Marx & Miller (2018) claim that the intrinsic scatter in the BCG stellar mass at fixed halo mass can be reduced if accounting for the magnitude gap. Finally, Harvey et al. (2017) predict a residual BCG wobbling in clusters due to previous major mergers.

Fig. 7 shows the relation between the BCG offset from the group X-ray peak/centre (r/R_{200}) as a function of the magnitude gap between the first and second brightest group galaxies within R_{200}. We note that the offset/magnitude gap estimation within $0.5R_{200}$ represents similar trends. We plot the offset–gap relation for groups at three different redshift ranges, $z = 0.0$–0.5 (black circles), $z = 0.5$–1.0 (red squares), and $z = 1.0$–1.5 (blue diamonds). We find that the BGG offset from the halo X-ray centre decreases as a function of increasing magnitude gap with no redshift-dependent trend.

In summary, we conclude that the BGG offset depends on the halo mass with a redshift-dependent trend. The BGG offset from the group X-ray centre also decreases with increasing r-band magnitude gap between the first and second ranked brightest group galaxies, suggesting that the BGG offset is an important observable that can be used to determine the group dynamical states. This parameter is not driven, e.g. by SNR in the observational data, and not driven by observational noise. The off-central BGGs probably reside in groups that are more likely to have experienced a recent halo merger or are undergoing a merger. The host groups of off-central BGGs generally include two massive luminous galaxies and they will possibly merge into one and probably get closer to the group's centre, expecting that the BGG offset will decrease with time as the group evolves dynamically.

5 DIFFERENCES IN THE STELLAR MASS DISTRIBUTION OF THE CENTRAL DOMINANT BGGS AND THE LARGE-OFFSET BGGS

This paper uses the physical properties of the galaxies from the COSMOS2015 catalogue presented by Laigle et al. (2016). The main improvement in this catalogue compared to previous COS-

MOS catalogue releases is the addition of new, deeper NIR and IR data from the UltraVISTA and SPLASH projects. The COSMOS2015 catalogue contains precise stellar masses for over half a million objects at the $\sim 2\,\mathrm{deg}^2$ COSMOS field. Including new $YJHK_s$ observations from the UltraVISTA-DR2 survey, Y-band observations from Subaru/Hyper-Suprime-Cam, and infrared data from the Spitzer Large Area Survey with the Hyper-Suprime-Cam Spitzer legacy programme, this highly optimized near-infrared-selected catalogue allows study of the evolution of galaxies and the environment effects in the early Universe. For more details on the stellar mass estimation and the physical properties of galaxies, the reader is referred to Laigle et al. (2016).

5.1 The BGG position within its host halo

The position of BGG in a group does not always correspond to the centre of the group potential well (Beers & Geller 1983; Zabludoff et al. 1993; Lazzati & Chincarini 1998; Lin & Mohr 2004; Von Der Linden et al. 2007; Skibba et al. 2010; Oliva-Altamirano et al. 2014). This is probably due to recently accreted relatively massive satellites that have not still merged and may still be growing (Skibba et al. 2010). These galaxy groups may also recently be dynamically relaxed. For a sample of massive and low-z clusters whose BCGs are generally central galaxies, such a selection may not affect the scientific conclusion. However, this selection criterion can significantly affect the scientific results reached on BGG properties and evolution. In this study, we use a clean sample of BGGs selected from (flag ≤ 3) groups and examine the BGG selection within three different radii ($0.5R_{500}$, R_{500}, and R_{200}). We investigate possible contamination of the BGG sample by the SBGG selected within the mentioned aperture sizes.

The upper panel of Fig. 8 presents the stellar mass distribution of BGGs (solid curves) and SBGGs (dashed curves) selected within $0.5R_{500}$, R_{500}, and R_{200}, respectively. The y-axis corresponds to the normalized count of BGGs/SBGGs ($n = N/N_{\rm tot}$). We find that distributions of the stellar mass of BGGs and SBGGs corresponding for each radius peak at $\log(M_*/M_\odot) \sim 11.1$–$11.4$ and $\log(M_*/M_\odot) \sim 10.7$–$11.0$, respectively. All distributions tend to skew to lower masses; however, the skewness increases with decreasing the aperture size from R_{200} to $0.5R_{500}$. In order to quantify possible contamination of the BGG sample by SBGG, we measure the BGG-to-SBGG ratio ($f = n_{\rm BGG}/n_{\rm SBGG}$) for each stellar mass bin. The ratio remains constant at ~ 0.5 for $0.5R_{500}$ and R_{500} and 0.4 for R_{200} at $\log(M_*/M_\odot) \leq 10.5$, then it increases for high masses. We find that the BGG selection could potentially be more contaminated at $\log(M_*/M_\odot) \leq 10.5$ and the probability of missing a true BGG increases from 40 to 50 per cent when the aperture size for choosing BGGs decreases from R_{200} to $0.5R_{500}$.

The lower left panel of Fig. 8 shows the stellar mass distribution of bona fide (true) BGGs (hereafter BGG$_T$). We have subtracted possible contamination of the BGG sample by SBGG. We also show the stellar mass distribution of BGGs (R_{200}) without subtracting the contamination. The y-axis corresponds to ($n_{\rm BGG} - f \times n_{\rm SBGG})/(1 - f)$. As is seen, the stellar mass distributions of bona fide BGGs selected from different apertures are approximately similar at $\log(M_*/M_\odot) > 10.5$. In other words, among BGG$_T$s there is no evidence for a BGG mass to be below $\log(M_*/M_\odot) \sim 10$, those below this mass are possibly misidentified BGGs. It is not expected that a galaxy with a stellar mass of $\log(M_*/M_\odot) \sim 8$–9 to be as a central group galaxy at $z < 1$, what is seen in the M_* distribution of BGGs selected within $0.5R_{500}$. In addition, we find no signifi-
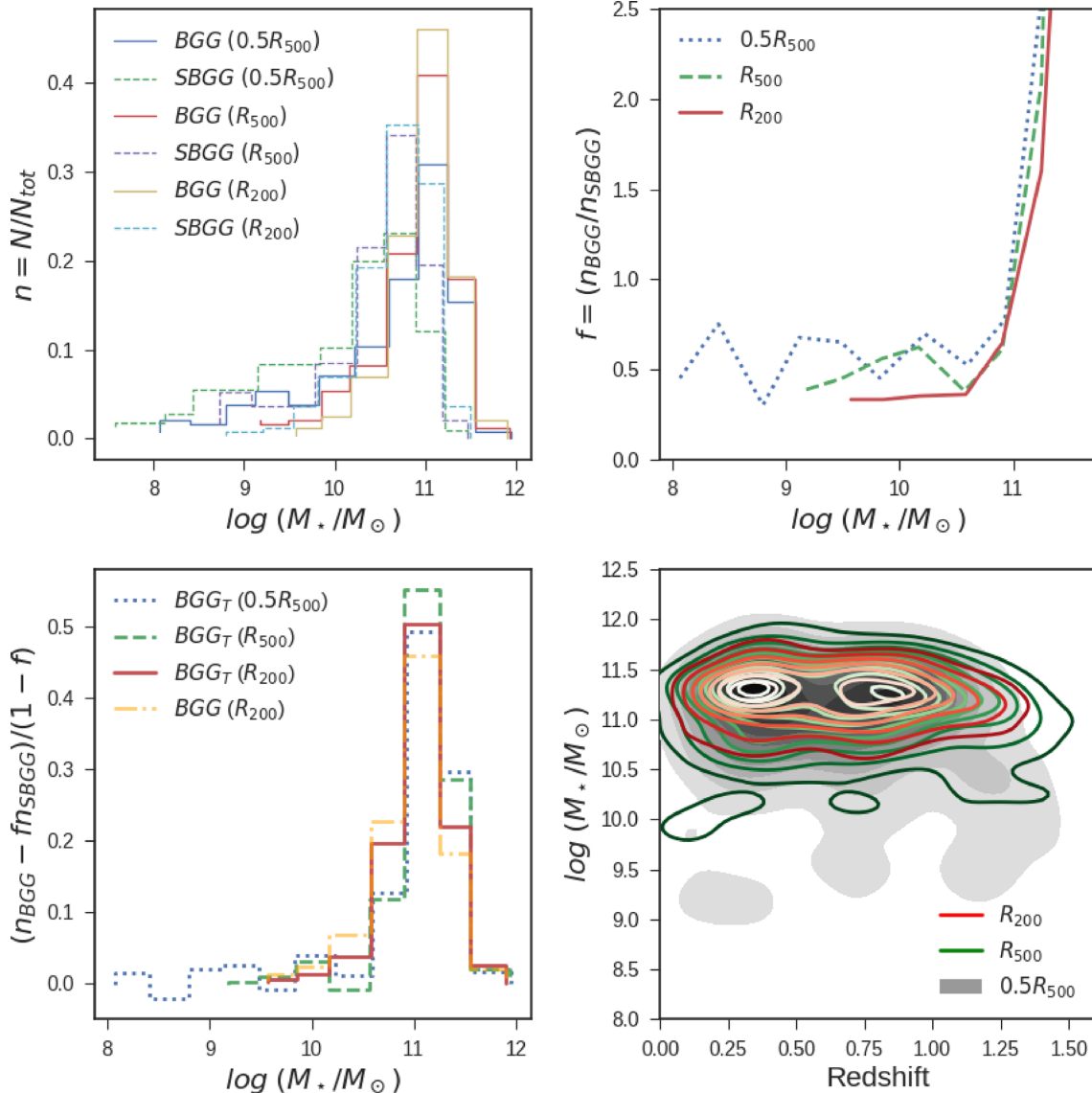
Figure 8. *Upper left panel:* The distribution of $\log(M_\star/M_\odot)$ for the full sample of BGGs (solid curves) and the SBGG (dashed curves) selected within three different apertures from the group X-ray centre: R_{200}, R_{500}, and $0.5R_{500}$. It appears the stellar mass distribution of the BGGs tends to skew to lower masses with decreasing the group radius from R_{200} to $0.5R_{500}$. *Upper right panel:* The BGG-to-SBGG ratio per stellar mass bin. The probability of missing a BGG increases from 40 to 50 per cent when the aperture size for BGG selection increases from $0.5R_{500}$ to R_{200}. *Lower left panel:* The stellar mass distribution of bona fide (true) BGGs (BGG$_T$) selected within R_{200} (solid red curve), R_{500} (dashed green curve), and $0.5R_{500}$ (dotted blue curve) after subtracting possible contamination by SBGGs. The yellow dot–dashed line shows the stellar mass distribution of BGGs selected within R_{200} without subtraction of any contamination. *Lower right panel:* The density map of the stellar mass versus redshift for BGGs selected within R_{200} (solid red contours), R_{500} (solid green contours), and $0.5R_{500}$ (shaded grey area). Both the panels show that by decreasing the group radius from R_{200} to smaller radii, e.g. $0.5R_{500}$, where BGGs are selected, a number of low-mass galaxies that are located in the central region of groups are chosen as BGGs while there are more massive galaxies a little farther from the group X-ray centre with no dependence on redshift.

cant difference between the mass distribution of BGG$_T$s and that of BGGs without subtraction of the contamination.

The density maps of the stellar mass of those BGGs versus redshift are also plotted in the lower right panel of Fig. 8. We find that by decreasing the group radius the stellar mass distribution of BGGs tends to skew to lower stellar masses. As an example, when selecting BGGs within $0.5R_{500}$ (even R_{500}), a number of low-mass satellite galaxies with $M_\star \sim 10^{8-9} M_\odot$ are chosen as BGGs in some groups while there are more massive bright galaxies at 100–300 kpc in these systems. After a careful inspection of groups and their associated BGGs, we conclude that the best radius for selecting BGGs

within our groups is R_{200} that approximately corresponds to the physical virial radius of haloes.

In order to test whether the stellar mass distributions of BGGs selected within $0.5R_{500}$, R_{500}, and R_{200} are drawn from the same distribution, we apply two-sided K–S test and measure the K–S statistics and p-values. Table 4 presents the K–S test results. We find that the stellar mass distribution for BGGs selected within R_{200} is slightly different from that of the BGGs selected within R_{500}. This difference increases when selecting BGGs within $0.5R_{500}$. However, we cannot reject the hypothesis that the distributions of the two samples of BGGs selected within R_{500} and $0.5R_{500}$ are the same.

Table 4. The results of two-sided K–S test to examine whether the stellar mass distributions of BGGs selected within $0.5R_{500}$, R_{500}, and R_{200} are drawn from the same distribution. Column 1 presents two samples that are compared. Columns 2 and 3 list the K–S statistics and *p*-values.

BGG samples	K–S statistics	*p*-value
(R_{200}, R_{500})	0.095	0.210
$(R_{200}, 0.5R_{500})$	0.244	7.138
$(R_{500}, 0.5R_{500})$	0.158	0.004

5.2 Distribution of the stellar mass of BGGs

This study aims to measure differences between the stellar mass distribution of the central dominant BGGs with an offset ≤0.2 with those BGGs with a large offset >0.2. We also compare the stellar mass distributions of BGGs with low and large offsets with the full sample of BGGs without considering offset.

In order to smooth the shape of the stellar mass distribution and minimize the effects (e.g., choice of binning) of using a histogram as a density estimator, we use the Kernel Density Estimation (KDE) technique (Rosenblatt 1956) and determine the PDF of $\log(M_\star/\mathrm{M}_\odot)$ using a so-called 'Gaussian' kernel.

Fig. 9 presents the smoothed distribution of $\log(M_\star/\mathrm{M}_\odot)$ of BGGs. Each panel, except for the lower-right panel, presents the $\log(M_\star/\mathrm{M}_\odot)$ distributions for a subsample of S-I to S-V. We show the $\log(M_\star/\mathrm{M}_\odot)$ distributions for BGGs with a low offset, BGGs with a large offset, and all BGGs with dashed, solid, and dotted black lines, respectively. The distributions of $\log(M_\star/\mathrm{M}_\odot)$ of the central and large-offset BGGs selected from the H15 SAMs are illustrated with dashed and solid magenta lines. We also show the distribution for the central BGGs from the G11 model with a dashed cyan line. The stellar mass distributions for the central and large-offset BGGs in the Magneticum simulation are plotted with dashed and solid green lines, respectively. The main findings of the stellar mass distribution of BGGs for S-V to S-I in Fig. 9 are summarized as follows:

(i) For S-V, we find that the stellar mass distribution of the central BGG approximately shows a single Gaussian distribution, while the distribution for BGGs with a large offset shows a second peak at around $\log(M_\star/\mathrm{M}_\odot) = 10.5$, and this causes the shape of the stellar mass distribution to deviate from a Gaussian distribution. Overall, we find a good agreement between model predictions and observations, and the deviation of the position of the peaks (mean stellar mass) among observations and predictions for central BGGs and those with a large offset is not significant.

The Magneticum simulation overestimates the stellar mass of both the central dominant BGGs and the large-offset BGGs in observations by ∼0.6 dex.

(ii) For S-IV, the shapes of $\log(M_\star/\mathrm{M}_\odot)$ distributions for all BGGs and BGGs with large observational offsets are similar to those for S-V; however, the height of the second peak seems to increase by a factor of 2. We observe that the distribution for the central BGGs in observations tends to skew to lower masses and the position of the centre of the peak moves to higher masses compared to the same for the S-V distribution and there is a deviance of the stellar mass evolution by ∼0.2 dex from $z = 1.3$ to 0.7. The mean of the stellar mass of central dominant is also higher than that of BGGs with a large offset by ∼0.2 dex, in agreement with prediction by H15. G11 and H15 similarly predict the stellar mass distribution of central BGGs and both models underpredict the mean stellar mass.

Just as for S-V, Magneticum simulation overpredicts the stellar mass of the central dominant and large-offset BGGs in observations by ∼0.4 dex.

(iii) For S-III, we determine a normal distribution for the stellar mass of central dominant BGGs when compared with S-IV. It also appears that the peak of this distribution becomes more flat and its position tends to move to lower values, indicating that the fraction of BGGs at the left-hand side of the distribution has been increased compared to that for S-IV. This can be explained by the infall of massive galaxies to the groups or group mergers at this epoch. For S-III, the stellar mass distributions for the central BGGs and the large-offset BGGs are approximately consistent. The G11 and H15 give good predictions for the position of the peak of the stellar mass distribution for the central BGGs. However, H15 underpredict the observed mean stellar mass for the large-offset BGGs by 0.3 dex.

Just as for S-V and S-IV, the Magneticum simulation overpredicts the stellar mass of the central dominant and large-offset BGGs in observations by about ∼0.4 dex.

(iv) For S-II, we find a significant evolution in the shape of the stellar mass distribution for both the central dominant BGGs and the large-offset BGGs. A second peak appears in the stellar mass distribution for central galaxies at $\log(M_\star/\mathrm{M}_\odot) = 10.5$, while the enhancements in the $\log(M_\star/\mathrm{M}_\odot)$ distribution for the large-offset BGGs at lower masses disappear and it roughly becomes as a normal distribution. We find that the observed mean stellar mass of the central dominant BGGs is higher than that of BGGs with a large offset of 0.5 dex. In the H15 prediction, this deviation is 0.25 dex. H15 well predict the mean stellar mass (the position of the centre of the peak) for BGGs with a large offset. Both H15 and G11 models underpredict the mean stellar mass of the dominant central BGGs for S-II by ∼0.4 dex.

It appears that the predictions by the Magneticum simulation become close to observation compared to those of the high-*z* subsamples. However, there are still ∼0.25 dex differences between the stellar mass of BGGs in the observations and this simulation.

(v) For S-I, the shape of the stellar mass distribution is similar for both of the central dominant BGGs and BGGs with large offsets, however that of the centrals spans a wide dynamic mass range. Both distributions represent deviation from the normal distribution on the left-hand tail at lower stellar masses. The sign of the presence of the second peak in this side of the distribution is evident. The height of the peak and its position are consistent for both the central BGGs and the BGGs with large offsets. We observe similar trends in model predictions; however, models underpredict the observed mean stellar mass by 0.5 dex.

The Magneticum simulation predicts the stellar mass distribution of both the central and large-offset BGGs for S-I remarkably well.

(vi) On the right-hand side of the bottom panel of Fig. 9, we show the stellar mass of BGGs with low offsets (black points) versus the redshift in observations. We also apply the KDE method and measure the corresponding density as shown with the shaded red contours (area). We determine the density for the central BGGs from the H15 model. The purple contours illustrate this density. We mention that G11 model also predicts in the same way as the H15 model. We find that these models overall underpredict the stellar mass of BGGs in observations. The green contours present the data for the central dominant BGGs in the Magneticum simulation.

(vii) According to our observations, we argue that BGG is not always at rest at the centre of potential well of a virialized halo. We conclude that the BGG offset from the X-ray centre of a group is
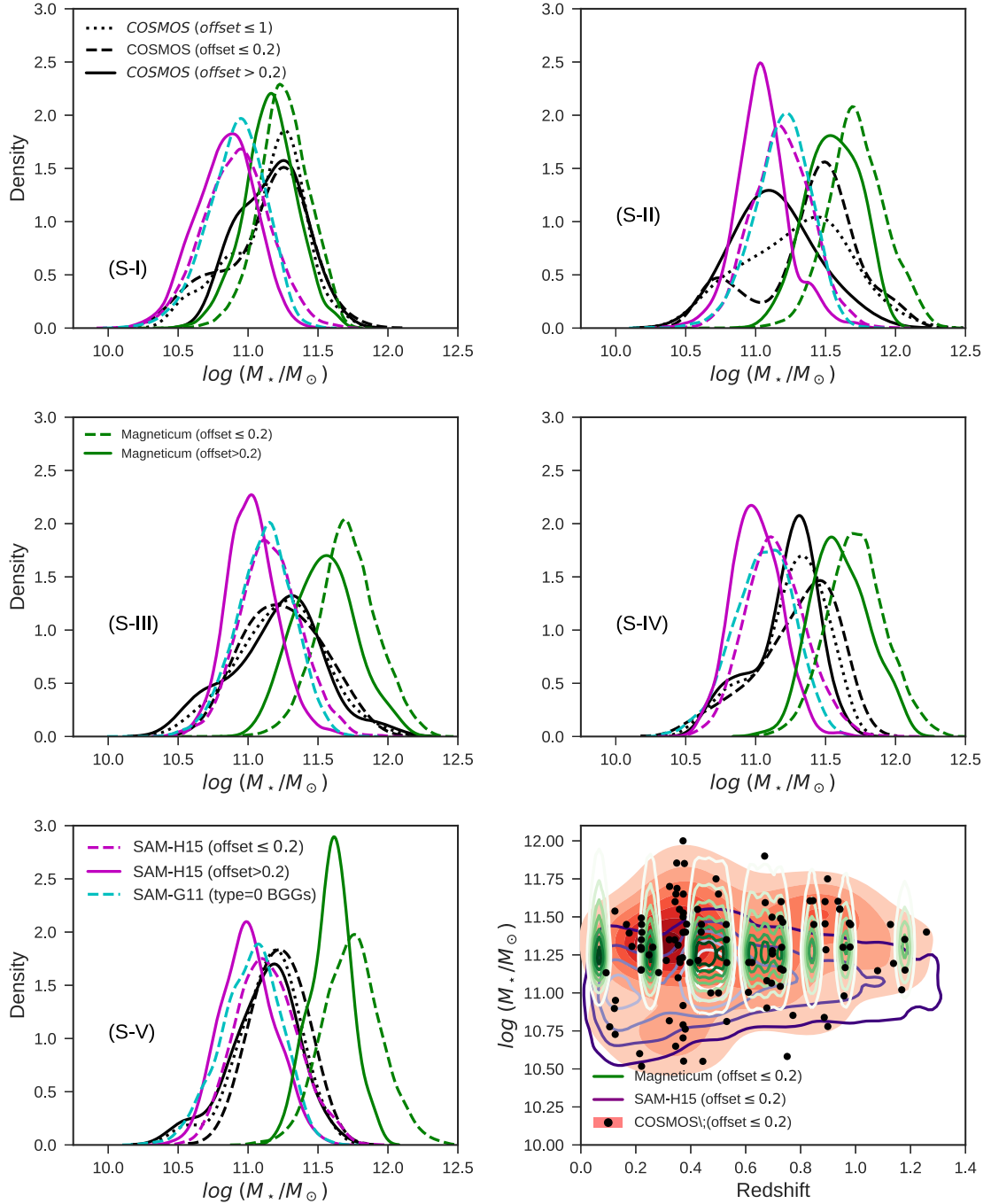
Figure 9. The smoothed distribution of $\log(M_\star/M_\odot)$ for the full sample of BGGs (dotted black line), BGGs with a low offset from the X-ray centre (offset $= \frac{r[\deg]}{R_{200}[\deg]} \leq 0.2$) (dashed black line), and BGGs with a large offset (offset >0.2), by Gaussian kernel density estimator. The smoothed stellar mass distributions of the central dominant BGGs and the large-offset BGGs predicted by H15 are plotted with dashed and solid magenta lines, respectively. The stellar mass distributions of the central dominant BGGs and the large-offset BGGs in the hydrodynamical simulation of Magneticum are plotted with dashed and solid green lines, respectively. The dashed cyan line shows the stellar mass distribution of the central BGGs (type $= 0$ galaxies) in the G11 SAM. The lower right panel presents $\log(M_\star/M_\odot)$ as a function of redshift. The density maps of BGGs with low offsets in observations are shown with the shaded red area. Black points present the stellar mass versus redshift for the central dominant BGGs (offset <0.2) in observations. The purple and green contours illustrate the density contours for the central BGGs in the H15 model and the Magneticum simulation, respectively.

an important observable and parameter, which is suggestive that it should be taken into account in galaxy formation model based on the CGP. The offset assumption can bring those model predictions more closer to the observed features of BGGs.

In summary, observations and models indicate that the central dominant BGGs are generally more massive than the BGGs with large offsets. We find systematic differences between model predictions and observations, which could have many reasons.

The simulations in general should capture this dynamical effect well, but the predicted X-ray emission (and therefore the definition of the centroid) could suffer from too simplistic assumptions going in here. Obviously, it could be also the action of the AGN that seems not to have been captured very well in the simulations. In addition, the contamination of AGNs or the contribution of ISM or metal lines in the colder phase could lead to more emission from the BGG in reality than predicted by the simplistic approach in the simulations, and therefore change the offset calculation. In observations, the samples are flux limited, so observations could be biased to cool-core systems at high redshifts.

5.3 The log-normal scatter in the stellar mass of BGGs at fixed halo mass and redshift

The stellar mass of central galaxies exhibits a tight relation with the halo mass of hosting haloes. This relation is an important observable and constraining this relation is a key way to examine model predictions, recognizing the role of different physical mechanisms (e.g. star formation and feedback from stellar evolution and AGN activity) in the formation of BGGs (Behroozi et al. 2010, 2013; Yang et al. 2012; Moster et al. 2013; Coupon et al. 2015). Both observations and models illustrate that there exists a scatter in the stellar mass of central galaxies at fixed halo mass. This is one of the main sources of difference between results, and the origin of this scatter is still an unresolved problem. In Gozaliasl et al. (2018), we showed that the scatter in the stellar mass of BGGs is higher than the prediction by the H15 SAM and the study based on abundance matching and HOD methods by, e.g. Coupon et al. (2015). The observed scatter increases with redshift from $\sigma_{\log M_\star} \sim 0.3$ at $z \sim 0.2$ to 0.5 at $z \sim 1.0$. Our measurements show a remarkable agreement with a recent study by Chiu et al. (2016), who measured the $M_\star$–M_{200} scaling relation for 46 X-ray groups detected in the *XMM–Newton*-Blanco Cosmology Survey (*XMM*-BCS) with a median halo mass of $8 \times 10^{13}\,\mathrm{M_\odot}$ at a median redshift of $z = 0.47$, finding a scatter of $\sigma_{\log M_\star | M_{500}} = 0.36^{+0.07}_{-0.06}$. In this study, we used data from different surveys and we measured the scatter for all BGGs as a whole.

Using this revised data of X-ray galaxy groups and BGGs in the COSMOS field, we recalculate the log-normal scatter in the stellar mass for the full sample of BGGs, and BGGs with low and large offsets at fixed redshift and halo mass. We investigate whether the offset between the position of the BGGs and the X-ray centres of their host haloes might have an impact on scattering the BGG mass.

Fig. 10 shows the log-normal scatter in stellar mass of BGGs as a function of redshift (upper panel) and halo mass M_{200} (lower panel). We note that the scatter corresponds to the standard deviation of $\log(M_\star/\mathrm{M_\odot})$ at a given redshift/halo mass range. The results for different subsamples are shown with different colours. To distinguish data points of BGGs with different offset values, we shift data along the x-axis by ± 0.03. We compare our results from the observations with predictions from the G11 and H15 SAMs. We determine scatter in the stellar mass of the central BGGs with an offset ≤ 0.2 (dashed magenta line) and BGGs with a large offset >0.2 (solid magenta line) in the H15 model and the central BGGs (type = 0) in the G11 model (dashed cyan line). The solid and dashed green lines illustrate the scatter in the stellar mass of the central and offset BGGs in the Magneticum simulation. In the upper panel of Fig. 10, we find that $\sigma_{\log M_\star}$ for all types of BGGs in terms of offset is generally consistent and the major differences in $\sigma_{\log M_\star}$ between the large-offset and low-offset BGGs are seen for
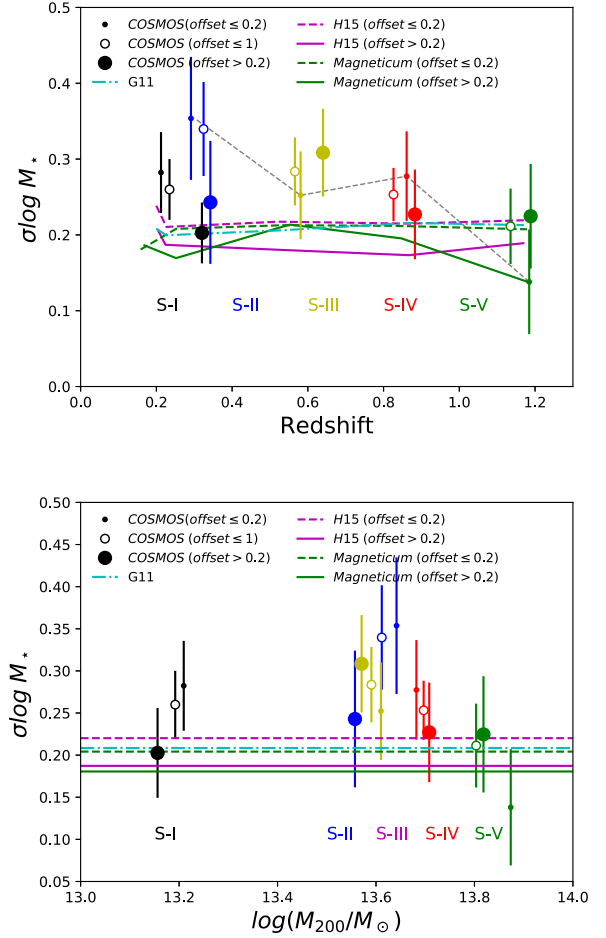
Figure 10. The scatter in the stellar mass of BGGs ($\sigma_{\log M_\star}$) as a function of redshift and halo mass. $\sigma_{\log M_\star}$ values for the full sample of BGGs, the central BGGs (offset $= \frac{r[\deg]}{R_{200}[\deg]} \leq 0.2$), and the large-offset BGGs (offset >0.2) in observations are plotted as the open circles, filled small circles, and filled large circles, respectively. Results for S-I to S-V subsamples are shown with black, blue, yellow, red, and green symbols, respectively. The horizontal dashed and solid magenta lines and the dash–dotted cyan line present constant scatter in the stellar mass of central dominant BGGs and BGG with large offsets from H15 model and the central BGGs (type = 0 galaxies) from the SAMs of G11, respectively. The solid and dashed green lines show the log-normal scatter in the stellar mass of the central dominant and large-offset BGGs in the Magneticum simulation.

S-IV, S-II, and S-I by approximately 0.1 dex, which is not significant within errors. $\sigma_{\log M_\star}$ for S-II to S-IV remains constant around $\sigma_{\log M_\star} \sim 0.30 \pm 0.07$ dex at $z < 1$, while $\sigma_{\log M_\star}$ for S-V drops to $\sigma_{\log M_\star} \sim 0.1 \pm 0.06$, indicating a redshift evolution between S-V and S-IV (from $z \sim 1.3$ to 0.7). Interestingly, when the current measurement of $\sigma_{\log M_\star}$ for S-V is compared with our previous measurement ($\sigma_{\log M_\star} \sim 0.5 \pm 0.09$) in Gozaliasl et al. (2018), we find that the current estimate of $\sigma_{\log M_\star}$ is much lower than the former estimate. This indicates that the quality of the galaxy stellar mass estimates in COSMOS is much better than the data of galaxies in *XMM*-LSS and AEGIS field, which we used in Gozaliasl et al. (2018). For S-I, we also have an improvement in our measurement compared to that in Gozaliasl et al. (2018) and find that the current estimate $\sigma_{\log M_\star}$ for S-I is in agreement with other subsamples of BGGs (e.g. S-II) at $z < 1$.

For the central dominant and large-offset BGGs selected from the H15 model, we estimate that $\sigma_{\log M_\star}$ remains constant with both redshift and halo mass at $\sigma_{\log M_\star} = 0.220$ and 0.187 dex, respectively. It appears that the scatter in the stellar mass of BGGs with a large offset in the H15 model is $\sim$0.04 dex less than that of the central BGGs in this model. The scatter in the stellar mass of central BGGs in the G11 prediction is $\sigma_{\log M_\star} = 0.208$ dex. Models are found to be in a good agreement with the data in observations within errors. In the lower panel of Fig. 10, we find no significant dependence of $\sigma_{\log M_\star}$ on halo mass, however, noting that the halo mass range of groups used in this analysis is too small. The scatters of the stellar mass of the central dominant (dashed green line) and the offset (solid green line) of BGGs in the Magneticum simulation are consistent observations within the errors and predictions from the H15 and G11 models. In the Magneticum simulation, we find that the scatter in the stellar mass of the large-offset BGGs increases slightly with redshift, which is in a good agreement with observations.

6 SUMMARY AND CONCLUSIONS

We present the revised catalogue of 247 X-ray groups of galaxies in the 2 deg^2 COSMOS field with $M_{200c} = 8 \times 10^{12}$–$3 \times 10^{14}$ M$_\odot$ at a redshift range of $0.08 \leq z < 1.3$. The main revisions are on the group X-ray centre using the combined data of the *XMM–Newton* and *Chandra* and the redshift based on the COSMOS2015 photometric redshifts catalogue (Laigle et al. 2016) and the COSMOS spectroscopic redshifts catalogue (Hasinger et al. 2018). We select the BGGs from our X-ray galaxy groups and define five subsamples (S-I to S-V) considering the halo mass and redshift of hosting groups such that four out of five have the same halo mass range. This definition allows us to investigate the stellar mass distribution of BGGs within haloes of similar masses, but at different redshifts. We study differences in the stellar mass distribution between the central dominant BGGs and BGGs with a large offset from the X-ray peak. The BGG offset is defined as the ratio of the separation between the position of this galaxy and the group X-ray centre to the group R_{200} radius. BGGs in each subsample are classified into three types based on the offset: the central dominant BGGs (offset ≤ 0.2), large-offset BGGs (offset >0.2), and full sample of BGGs (offset ≤ 1). We determine the log-normal scatter in the stellar mass of BGGs. We interpret our results with predictions from two SAMs of H15 and G11 implemented based on the Millennium simulation and the results from the hydrodynamical simulation of Magneticum. The summary of our findings is as follows:

(i) We inspect the BGG selection within different radii from the X-ray centre of haloes (R_{200}, R_{500}, $0.5R_{500}$) and find that the best aperture for the BGG selection for groups with $M_{200} \sim 10^{13-14}$ M$_\odot$ is R_{200}. By decreasing the aperture from R_{200} to $0.5R_{500}$, the BGG stellar mass tends to skew towards low masses and the probability of missing true BGGs increases from 40 to 50 per cent. When selecting BGGs within $0.5R_{500}$, consequently, for a number of groups, centrally located low-mass satellite galaxies with $M_* \sim 10^{8-9}$ M$_\odot$ are selected as BGGs while there are more massive galaxies at 100–300 kpc, although the stellar mass distributions of the true (bona fide) BGGs selected within the mentioned apertures are similar above $M_* \sim 10^{10.5}$ M$_\odot$.

(ii) We find that the BGG offset decreases by a factor of 3 from $z = 1.3$ to the present day. We visually inspect the multiband images of groups having BGGs with large offsets and find that they generally include two massive and luminous galaxies. We conclude that these bright group members finally merge into one with time

and the newly formed BGG becomes closer to the host group X-ray centre.

(iii) We measure the *r*-band magnitude gap between the first and second brightest group galaxies within R_{200} and investigate its relation with the offset of the first BGG from the X-ray centre. We find that the offset decreases as a function of increasing magnitude gap with no considerable redshift-dependent trend.

(iv) We classified our sample of groups into three redshift bins, $z = 0.0$–0.5, 0.5–1.0, and 1.0–1.5, and selected clean groups in which we are able to define their X-ray centres. We found that the BGG offset from the group's X-ray centre decreases as a function of increasing group total mass (M_{200}) and the slope of the relation increases with increasing redshift. We show that the offset is not an effect driven by lower SNR and it shows no dependence on the X-ray flux and flux significance.

(v) We applied the normality test and find that the $\log(M_\star/\mathrm{M}_\odot)$ distributions for the full sample of BGGs for S-I, S-III, and SIV deviate a little from a normal distribution. This deviation in the shape of the stellar mass distribution is due to the deviation of the shape of the stellar mass distribution of BGGs with a large offset, in particular, at $z > 0.4$. However, at $z < 0.4$, the distribution of BGGs with a low offset for S-II leads the stellar mass distribution of the full sample of BGGs to deviate from a Gaussian distribution. We observe a second peak in the stellar mass distribution of the central dominant BGGs for S-II at $z < 0.4$.

(vi) By comparing the $\log(M_\star/\mathrm{M}_\odot)$ distribution between BGGs with a low offset with that of BGGs with a large offset, we conclude that the central BGGs are not evolving in the same fashion as BGGs with large offsets. Clearly, the differences between stellar mass distributions of BGGs with small and large offsets suggest that the offset is an important observable that must be taken into account in modelling BGGs/BCGs and hosting haloes as well. We believe that there are several astrophysical phenomena such as major merger, group/halo merger, and infalling massive galaxies into a system, all can lead to a large offset among the BGG position and the group X-ray centre.

(vii) Using our unique sample of BGGs, we determine a constant log-normal scatter in the stellar mass of BGGs, $\sigma_{\log M_\star} \sim 0.30 \pm 0.07$ dex, at $z < 1.0$ with no significant dependence on the BGG offset from the group X-ray centre. This scatter interestingly decreases to $\sigma_{\log M_\star} \sim 0.10 \pm 0.06$ at $z = 1.0$–1.3 for our S-V subsample, indicating a little redshift evolution from $z = 1.3$ to 0.17. The $\sigma_{\log M_\star}$ that we measure here is up to 0.15 dex less than that we estimate in our recent measurement (Gozaliasl et al. 2018) in the same redshift and halo mass ranges. We conclude that the high-quality multibands data of COSMOS effectively decrease bias in the stellar mass measurement and mixing low- and high-quality data from different surveys may lead to a large bias and scatter in the $\sigma_{\log M_\star}$ measurement, even if a similar method is used for estimating the stellar mass of galaxies from different surveys. Multiband observations and a precise redshift determination of galaxies are vital in measuring their stellar properties.

(viii) We find that the scatter in the stellar mass of BGGs does not depend significantly on the BGG offsets from the group X-ray centres.

(ix) By comparing our results with those from two SAMs of H15 and G11 and the hydrodynamical simulation of Magneticum, we conclude that models have generally captured the observed trends. Notably, we find that the mean stellar mass of the central dominant BGGs is higher than that of the large-offset BGGs in a good agreement with model predictions. However, there is still a systematic difference between the predictions from simulations and observations, which can arise for several reasons. For instance, the action of

the AGN seems to have not been captured very well in the simulations. In addition, the contamination of AGN or the contribution of ISM or metal lines in the colder phase could lead to more emission from the BGG in reality than predicted by the simplistic approach in the simulations, and therefore change the offset calculation. In the observations, the samples are flux limited, so observations could be biased to cool-core systems at high redshifts.

REFERENCES

Allevato V. et al., 2012, ApJ, 758, 47
Barnes J., 1985, MNRAS, 215, 517
Barnes J. E., 1989, Nature, 338, 123
Beers T. C., Geller M. J., 1983, ApJ, 274, 491
Beers T. C., Flynn K., Gebhardt K., 1990, AJ, 100, 32
Behroozi P. S., Conroy C., Wechsler R. H., 2010, ApJ, 717, 379
Behroozi P. S., Wechsler R. H., Conroy C., 2013, ApJ, 770, 57
Bower R. G., Benson A. J., Malbon R., Helly J. C., Frenk C. S., Baugh C. M., Cole S., Lacey C. G., 2006, MNRAS, 370, 645
Carnevali P., Cavaliere A., Santangelo P., 1981, ApJ, 249, 449
Cavaliere A., Santangelo P., Tarquini G., Vittorio N., 1986, ApJ, 305, 651
Ceraj L. et al., 2018, A&A, in press
Chandrasekhar S., 1943, ApJ, 97, 255
Chiu I. et al., 2016, MNRAS, 458, 379
Civano F. et al., 2016, ApJ, 819, 62
Cole S., Lacey C. G., 1996, MNRAS, 281, 716
Comparat J. et al., 2015, A&A, 575, A40
Connelly J. L. et al., 2012, ApJ, 756, 139
Coupon J. et al., 2015, MNRAS, 449, 1352
Cui W. et al., 2013, MNRAS, 437, 816
De Lucia G., Blaizot J., 2007, MNRAS, 375, 2
Diaferio A., Kauffmann G., Balogh M. L., White S. D. M., Schade D., Ellingson E., 2001, MNRAS, 323, 999
Dolag K., Borgani S., Murante G., Springel V., 2009, MNRAS, 399, 497
Dolag K., Murante G., Borgani S., 2010, MNRAS, 405, 1544
Elvis M. et al., 2009, ApJS, 184, 158
Erfanianfar G. et al., 2013, ApJ, 765, 117
Finoguenov A. et al., 2007, ApJS, 172, 182
Finoguenov A. et al., 2009, ApJ, 704, 564
Finoguenov A. et al., 2010, MNRAS, 403, 2063
Finoguenov A. et al., 2015, A&A, 576, A130
George M. R. et al., 2011, ApJ, 742, 125
Golden-Marx J. B., Miller C. J., 2018, ApJ, 860, 2
Gozaliasl G. et al., 2014a, A&A, 566, A140
Gozaliasl G. et al., 2018, MNRAS, 475, 2787
Gozaliasl G., Khosroshahi H. G., Dariush A. A., Finoguenov A., Jassur D. M. Z., Molaeinezhad A., 2014b, A&A, 571, A49
Gozaliasl G., Finoguenov A., Khosroshahi H. G., Mirkazemi M., Erfanianfar G., Tanaka M., 2016, MNRAS, 458, 2762
Guo Q. et al., 2011, MNRAS, 413, 101 (G11)
Harvey D., Courbin F., Kneib J. P., McCarthy I. G., 2017, MNRAS, 472, 1972

Hasinger G. et al., 2018, ApJ, 858, 77
Henriques B., White S. D. M., Thomas P. A., Angulo R. E., Guo Q., Lemson G., Wang W., 2017, MNRAS, 469, 2626
Henriques B. M. B., White S. D. M., Thomas P. A., Angulo R. E., Guo Q., Lemson G., Springel V., 2013, MNRAS, 431, 3373
Henriques B. M. B., White S. D. M., Thomas P. A., Angulo R., Guo Q., Lemson G., Springel V., Overzier R., 2015, MNRAS, 451, 2663 (H15)
Hirschmann M., Dolag K., Saro A., Bachmann L., Borgani S., Burkert A., 2014, MNRAS, 442, 2304
Ilbert O. et al., 2006, A&A, 457, 841
Ilbert O. et al., 2008, ApJ, 690, 1236
Ilbert O. et al., 2013, A&A, 556, A55
Jones C., Forman W., 1984, ApJ, 276, 38
Jones L. R., Ponman T. J., Horton A., Babul A., Ebeling H., Burke D. J., 2003, MNRAS, 343, 627
Karim A. et al., 2011, ApJ, 730, 61
Kartaltepe J. S. et al., 2010, ApJ, 721, 98
Kettula K. et al., 2015, MNRAS, 451, 1460
Khosroshahi H. G., Gozaliasl G., Rasmussen J., Molaeinezhad A., Ponman T., Dariush A. A., Sanderson A. J. R., 2014, MNRAS, 443, 318
Kochanek C. S., 1995, ApJ, 445, 559
Komatsu E. et al., 2011, ApJS, 192, 18
Kravtsov A. V., Berlind A. A., Wechsler R. H., Klypin A. A., Gottlöber S., Allgood B., Primack J. R., 2004, ApJ, 609, 35
Kriek M. et al., 2015, ApJS, 218, 15
Krogager J. K., Zirm A. W., Toft S., Man A., Brammer G., 2014, ApJ, 797, 17
Laigle C. et al., 2016, ApJS, 224, 24
Lavoie S. et al., 2016, MNRAS, 462, 4141
Lazzati D., Chincarini G., 1998, A&A, 339, 52
Leauthaud A. et al., 2010, ApJ, 709, 97
Leauthaud A. et al., 2012, ApJ, 746, 95
Le Fèvre O. et al., 2015, A&A, 576, A79
Lilly S. J. et al., 2007, ApJS, 172, 70
Lin Y.-T., Mohr J. J., 2004, ApJ, 617, 879
Lopes P. A. A., Trevisan M., Laganá T. F., Durret F., Ribeiro A. L. B., Rembold S. B., 2018, MNRAS, 478, 5473
Mamon G. A., 1987, ApJ, 321, 622
Mamon G. A., 1992, ApJ, 401, L3
Marchesi S. et al., 2016, ApJ, 817, 34
Matthee J., Schaye J., Crain R. A., Schaller M., Bower R., Theuns T., 2017, MNRAS, 465, 2381
McCracken H. J. et al., 2012, A&A, 544, A156
More S., Van Den Bosch F. C., Cacciato M., Mo H. J., Yang X., Li R., 2008, MNRAS, 392, 801
Moster B. P., Somerville R. S., Maulbetsch C., Van den Bosch F. C., Macciò A. V., Naab T., Oser L., 2010, ApJ, 710, 903
Moster B. P., Naab T., White S. D. M., 2013, MNRAS, 428, 3121
Nayyeri H. et al., 2017, ApJS, 228, 7
Oliva-Altamirano P. et al., 2014, MNRAS, 440, 762
Onodera M. et al., 2012, ApJ, 755, 26
Ponman T. J., Allan D. J., Jones L. R., Merrifield M., McHardy I. M., Lehto H. J., Luppino G. A., 1994, Nature, 369, 462
Postman M., Lauer T. R., 1995, ApJ, 440, 28
Raouf M., Khosroshahi H. G., Ponman T. J., Dariush A. A., Molaeinezhad A., Tavasoli S., 2014, MNRAS, 442, 1578
Remus R.-S., Dolag K., Hoffmann T. L., 2017, Galaxies, 5, 49
Roseboom I. G. et al., 2012, MNRAS, 426, 1782
Rosenblatt M., 1956, Ann. Math. Stat., 27, 832
Sanderson A. J. R., Edge A. C., Smith G. P., 2009, MNRAS, 398, 1698
Scoville N. et al., 2007, ApJS, 172, 1
Sheldon E. S. et al., 2009, ApJ, 703, 2232
Silverman J. D. et al., 2015, ApJS, 220, 12
Skibba R. A., Sheth R. K., 2009, MNRAS, 392, 1080
Skibba R. A., van den Bosch F. C., Yang X., More S., Mo H., Fontanot F., 2010, MNRAS, 410, 417
Springel V. et al., 2005, Nature, 435, 629
Springel V., Hernquist L., 2003, MNRAS, 339, 289

Springel V., White S. D. M., Tormen G., Kauffmann G., 2001, MNRAS, 328, 726

Teklu A. F., Remus R.-S., Dolag K., Beck A. M., Burkert A., Schmidt A. S., Schulze F., Steinborn L. K., 2015, ApJ, 812, 29

Tinker J. L., Conroy C., Norberg P., Patiri S. G., Weinberg D. H., Warren M. S., 2008, ApJ, 686, 53

Tornatore L., Borgani S., Dolag K., Matteucci F., 2007, MNRAS, 382, 1050

Trevisan M., Mamon G. A., 2017, MNRAS, 471, 2022

van den Bosch F. C., Aquino D., Yang X., Mo H. J., Pasquali A., McIntosh D. H., Weinmann S. M., Kang X., 2008, MNRAS, 387, 79

Vikhlinin A., McNamara B. R., Forman W., Jones C., Quintana H., Hornstrup A., 1998, ApJ, 502, 558

Von Der Linden A., Best P. N., Kauffmann G., White S. D. M., 2007, MNRAS, 379, 867

Wang T. et al., 2016, ApJ, 828, 56

White S. D. M., Rees M. J., 1978, MNRAS, 183, 341

Yang X., Mo H. J., van den Bosch F. C., Pasquali A., Li C., Barden M., 2007, ApJ, 671, 153

Yang X., Mo H. J., van den Bosch F. C., 2009, ApJ, 695, 900

Yang X., Mo H. J., van den Bosch F. C., Zhang Y., Han J., 2012, ApJ, 752, 41

Zabludoff A. I., Geller M. J., Huchra J. P., Ramella M., 1993, AJ, 106, 1301

Zabl J. F., 2015, PhD thesis, The Niels Bohr Institute, Faculty of Science, University of Copenhagen

SUPPORTING INFORMATION

Supplementary data are available at *MNRAS* online.

Table 2. The revised catalogue of X-ray galaxy groups in 2 deg^2 of the COSMOS field, which was previously presented by Finoguenov et al. (2007) and George et al. (2011).

Please note: Oxford University Press is not responsible for the content or functionality of any supporting materials supplied by the authors. Any queries (other than missing material) should be directed to the corresponding author for the article.

[1]*Finnish centre for Astronomy with ESO (FINCA), University of Turku, Väisäläntie 20, FI-21500 PIIKKIÖ, Finland*

[2]*Department of Physics, University of Helsinki, PO Box 64, FI-00014, Helsinki, Finland*

[3]*Helsinki Institute of Physics, University of Helsinki, PO Box 64, FI-00014, Helsinki, Finland*

[4]*Max Planck-Institute for Extraterrestrial Physics, PO Box 1312, Giessenbachstr. 1., D-85741 Garching, Germany*

[5]*School of Astronomy, Institute for Research in Fundamental Sciences (IPM), Tehran, 19395-5531 Iran*

[6]*Argelander-Institut für Astronomie, Universität Bonn, Auf dem Hügel 71, D-53121 Bonn, German*

[7]*National Astronomical Observatory of Japan, 2-21-1 Osawa, Mitaka, Tokyo 181-8588, Japan*

[8]*Aix Marseille Université, CNRS, Laboratoire ďAstrophysique de Marseille, UMR 7326, F-13388 Marseille, France*

[9]*CNRS, UMR 7095 and UPMC, Institut ďAstrophysique de Paris, 98bis boulevard Arago, F-75014 Paris, France*

[10]*Physics Department, University of Miami, Knight Physics Building, Coral Gables, FL 33124, USA*

[11]*Universitäts-Sternwarte München, Scheinerstr. 1, D-81679 München, Germany*

[12]*Max Planck Institut for Astrophysics, D-85748 Garching, Germany*

[13]*CEA Saclay, Laboratoire AIM-CNRS-Université Paris Diderot, Irfu/SAp, Orme des Merisiers, F-91191 Gif-sur-Yvette, France*

[14]*European Space Astronomy Centre (ESA/ESAC), Director of Science, E-28691 Villanueva de la Cañada, Madrid, Spain*

[15]*IPAC, Mail Code 314-6, California Institute of Technology, 1200 East California Boulevard, Pasadena, CA 91125, USA*

[16]*Cosmic Dawn centre (DAWN), Niels Bohr Institute, University of Copenhagen, Juliane Maries vej 30, DK-2100 Copenhagen, Denmark*

[17]*Sub-department of Astrophysics, University of Oxford, Keble Road, Oxford OX1 3RH, UK*

[18]*California Institute of Technology, 1200 E. California Boulevard, Pasadena, CA 91125, USA*

[19]*Harvard-Smithsonian centre for Astrophysics, 60 Garden Street, Cambridge, MA 02138, USA*

[20]*Department of Physics and Astronomy, University of Hawaii at Hilo, 200 W. Kawili Street, Hilo, HI 96720, USA*

[21]*Department of Physics and Astronomy, University of Waterloo, 200 University Avenue West, Waterloo, Ontario, Canada N2L 3G1, Canada*

[22]*Institute for Astronomy, University of Hawaii at Manoa, Honolulu, HI 96822, USA*

[23]*University of Paris Denis Diderot, University of Paris Sorbonne Cité (PSC), F-75205 Paris Cedex 13, France*

[24]*Sorbonne Université, Observatoire de Paris, Université PSL, CNRS, LERMA, F-75014 Paris, France*

[25]*Jet Propulsion Laboratory, Cahill centre for Astronomy and Astrophysics, California Institute of Technology, 4800 Oak Grove Drive, Pasadena, California, CA 91125, USA*

[26]*INAF-Osservatorio Astronomico di Brera, via Brera 28, I-20122 Milano, Italy*

[27]*Institute for Astronomy, ETH Zurich, CH-8093 Zurich, Switzerland*

[28]*Cosmic Dawn Center (DAWN), Niels Bohr Institute, University of Copenhagen, DK-2100 Copenhagen ø; DTU-Space, Technical University of Denmark, DK-2800 Kgs. Lyngby, Denmark*

This paper has been typeset from a TEX/LATEX file prepared by the author.